Comparison of Motion Controllers for a Flexure-Based Precision Manipulator

by
D. W. Vogel, BSc

Faculty of Engineering Technology
Precision Engineering

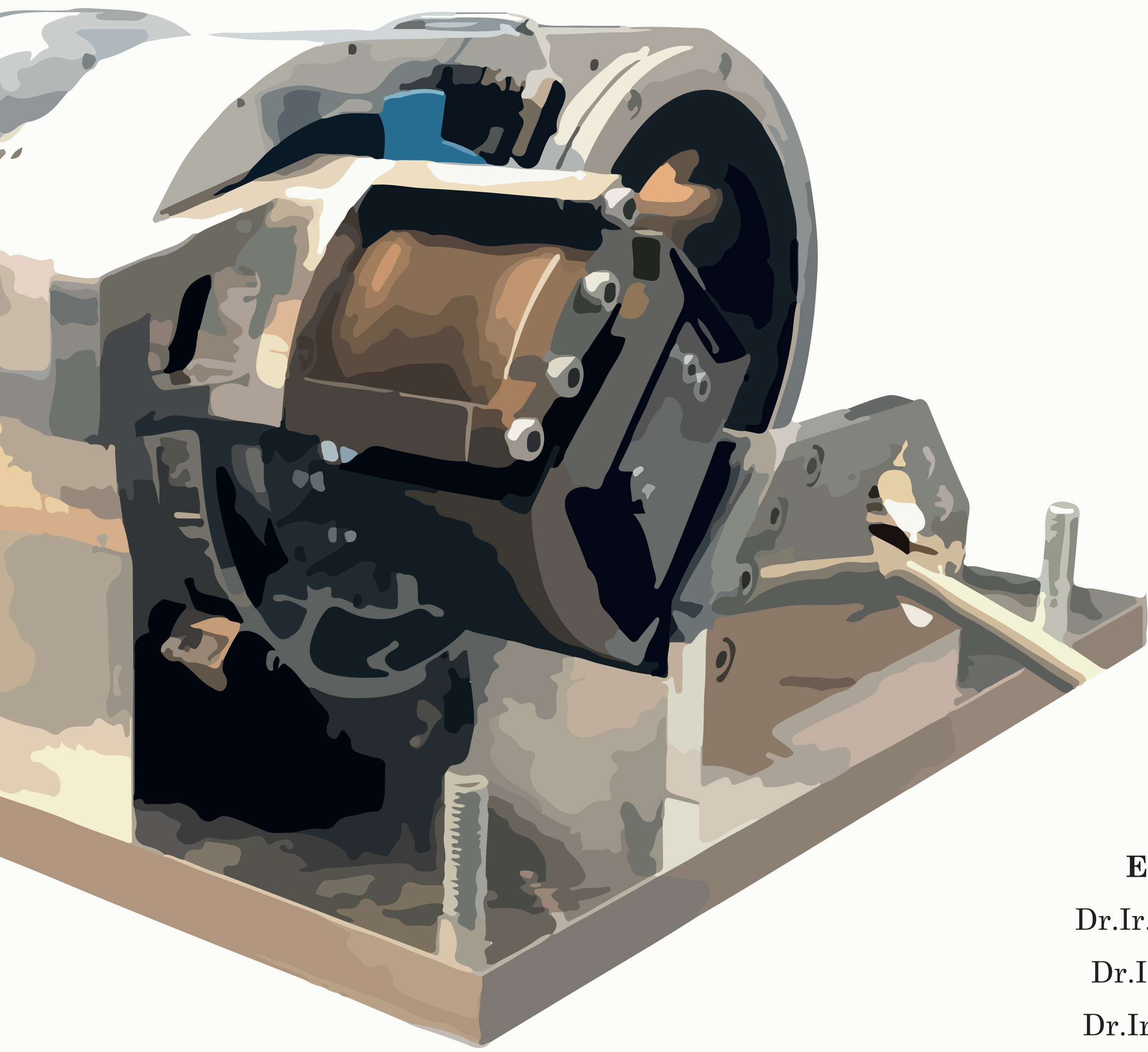

Exam Committee
Dr.Ir. W.B.J. Hakvoort
Dr.Ir. R.G.K.M. Aarts
Dr.Ir. A.Q.L. Keemink

Document nummer
ET/19-TM5860

UNIVERSITY OF TWENTE.

Comparison of Motion Controllers for a Flexure-Based Precision Manipulator

MASTER'S THESIS

BY

DAVE WILLIAM VOGEL

BORN ON 10^{TH} OF AUGUST 1995 IN HENGELO (OV), THE NETHERLANDS

JUNE, 2019

Examination Committee:
Dr.Ir. W.B.J. Hakvoort
Dr.Ir. R.G.K.M. Aarts
Dr.Ir. A.Q.L. Keemink

UNIVERSITY OF TWENTE
Faculty of Engineering Technology
Structural dynamics, acoustics and control
Department of Mechanics of Solids, Surfaces, and Systems - MS^3

CONTENTS

SUMMARY

Recently, the Precision Engineering group at the University of Twente designed a 6-DoF 6-RSS manipulator based on large stroke flexure hinges. The end-effector of this manipulator connects to the fixed world through a set of six parallel arms. The manipulator should be capable of a setpoint repeatability of $50\ \mathrm{nm}$, which due to the flexures and therefore lack of friction, has to be enabled by a feedback controller.

In this work, four different feedback controllers (PID, H_2, STSMC, and ADRC) are compared in their ability to maintain a non-equilibrium position for a single 1-DoF arm of this manipulator. This is a challenging control problem due to the high stiffness and lack of friction and a self-locking drive. H_2 control is found to have the best standstill performance with an RMS position error of $160\ \mathrm{nm}$ at the end-effector.
The comparison of the feedback controllers is extended by comparing their performance in tracking and disturbance rejection. The tracking performance is tested using different levels of feedforward of the system's dynamics, such that insight in their performance for different types of disturbances is gained. When utilizing all the information regarding the system's dynamics, H_2 has the best tracking performance. When less of the system dynamics is implemented in the feedforward, PID has the best tracking performance. For the disturbance rejection, PID and ADRC have the best performance.

Furthermore, an analysis of the disturbances on the manipulator is performed. The primary sources of disturbances are found to be the motor driver, cogging of the permanent magnet synchronous motor, and the hysteresis loop. The disturbance caused by the motor drive originates from the current ripple caused by the PWM signal and the current sensor. The cogging is determined using an analytical model, which is verified by a finite element analysis, which explained one of the two harmonics found. The other harmonic found has a manufacturing origin. The last disturbance source found is the hysteresis loop, which is believed to be of an electrical origin. The analysis showed that the loop is dependent on the sign of the velocity.

Comparison of Motion Controllers for a Flexure-Based Precision Manipulator

Dave Vogel [1]

[1]University of Twente, Netherlands

For a flexure-based precision manipulator, four different feedback controllers (PID, H_2, STSMC, and ADRC) are compared. Their performance in maintaining a non-equilibrium position for a system without friction is measured, for which H_2 control is found to have the best standstill performance of 160 nm at the end-effector. These controllers are, furthermore, tested for their performance in tracking and disturbance rejection. For the tracking performance, different levels of feedforward based on the system's dynamics are tested to give insight into the performance of the controllers. When all the system information is used H_2 yields the best tracking results, otherwise PID outperforms the other controllers. For the disturbance rejection, PID or ADRC have the best performance.

***Index Terms*—Feedback control comparison, PID, H_2, STSMC, ADRC, Feedforward, Tracking, Disturbance Rejection, Precision Systems.**

Introduction and Background

For many application, e.g. in the semiconductor industry and optics, the ever demanding increase in positioning performance results that bearing based devices are no longer up to the task due the their friction. Therefore, to meet tomorrows requirements, a novel flexure-based manipulator is designed.

Flexure-based manipulators allow for high-precision positioning due to the absence of play and friction. However, conventional flexure-based manipulators only allow small motions. Larger motions induce nonlinear and coupled stiffness behaviour of the flexures, which requires complex analysis, design, and optimization. This complex behaviour can be modelled by sophisticated tools to design and optimize large stroke flexures [1], which enables the design of a large-stroke spherical joint [2]. The ability to design and model large stroke joints ignited the idea to develop a fully flexure-based 6-DoF manipulator with a high stroke over reproducibility ratio [3].

A previous flexure-based 6-DoF manipulator design, the Commander6 built by Pyschny in 2013 [4], combines a flexure mechanism with piezo-stages with roller bearings. That system has a repeatability of 50 nm which is below commercially available micro positioners listed in [4] that have a repeatability down to 200 nm. On the other hand, its workspace (maximum directional stroke ± 4.5 mm), is much smaller than the workspace of commercially available manipulators.

The novel design presented in [3] and utilized in this paper, combines a large workspace with low repeatability. The fully flexure-based design, in combination with direct drive actuation and contact-less sensing, results in the absence of friction and play. As a result, the dynamics of the manipulator are expected to be continuous and well predictable. The design is depicted in Fig. 1. Its required workspace is a cube with sides of 100 mm centred around the midpoint of the platform. Furthermore, it should be able to rotate $\pm 20°$ about the horizontal axes and $\pm 18°$ about the vertical axis. The desired repeatability is 50 nm. Moreover, it should be able to reach accelerations up to $50\ \mathrm{m\,s^{-2}}$.

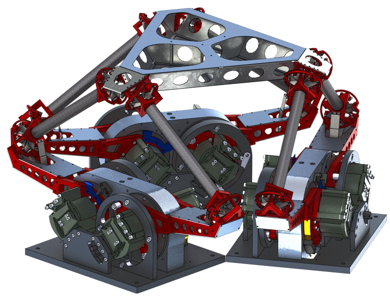

Fig. 1. The novel flexure-based 6-$\underline{R}$SS manipulator [3].

The unique aspects of the system, the combination of the lack of friction, and a self-locking drive together with being flexure-based, result in the absence of an equilibrium position in the workspace. Furthermore, disturbances that are conventionally negligible in comparison to friction become relavant. Therefore, appropriate feedback control is required to realise the set specifications for the novel manipulator. In particular, the realisation of the tight standstill performance results in a challenging control problem. Therefore an appropriate feedback controller has to be chosen. The (feedback) control of manipulators is a well-covered area of research, and many control strategies have been proposed in literature. Various one-to-one comparisons have been found: PID vs. SMC [5]; SMC vs. STSMC [6]; PID vs. H_2 [7]; and lastly, PID vs. Linear ADRC [8]. However, a good comparison of the performance of the various methods has not been found in literature. Furthermore, it is not fully clear how the presence of stiffness and the absence of friction affects their performance.

The contribution of this paper is an extensive comparison between PID, H_2, Super Twisting Sliding Mode (STSMC), Linear Active Disturbance Rejection Control (LADRC), and

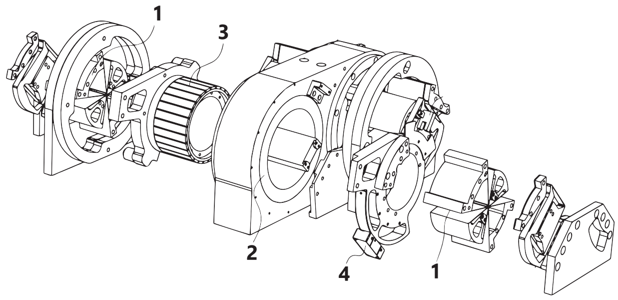

Fig. 2. An exploded view of the 1-DoF base joint [3]. 1) The butterfly flexure. 2) The stator of the direct drive motor. 3) The rotor of the direct drive motor. 4. illustrates the position of the encoder.

Nonlinear ADRC (NLADRC) for the considered manipulator. In particular, the suitability of the methods for high standstill accuracy in the presence of stiffness and absence of self-locking and friction are investigated. Furthermore, disturbance rejection and tracking with or without feedforward are evaluated.

The first section presents the one degree of freedom (1-DoF) system, which is built as a proof of concept of the more extensive 6-DoF system introduced earlier. Furthermore, this 1-DoF manipulator is used for the comparison of the different feedback controllers. The second section introduces the various feedback controllers. Furthermore, the feedforward control is described, which is added to the feedback controllers to show the combinatory effect on tracking performance. The feedforward is based on the identification of the system's dynamics. The third section describes the experimental results of the feedback controllers for their performance in standstill, tracking and disturbance rejection. This paper ends with conclusions and a discussion on possible improvements.

System Description

To prove the concept of the complete system, the actuated 1-DoF rotational joint at the base is built. This allows to test the behaviour of the base joint and compare control algorithms for their performance. The 1-DoF system is depicted in Fig. 2. Furthermore, an additional load of $1.46\ \mathrm{kg}$ can be mounted to mimic the load of the full system. The joint has similar characteristics as the 6-DoF system as it is a system without mechanical hysteresis, Therefore, enabling high precision, high repeatability and overall high performance. The design goals for the 6-DoF system have been converted for the 1-DoF system by dividing the earlier mentioned specifications with the transmission ratio, l, of $0.1\ \mathrm{m}$. This translates to a resolution of $500\ \mathrm{nrad}$, rotations of $\pm 0.52\ \mathrm{rad}$ ($30°$) and acceleration of $500\ \mathrm{rad\,s^{-2}}$ for the 1-DoF system.

The components used to control the 1-DoF system are listed in Table I, including their main specifications. The encoder is positioned at the base. Its readout strip is mounted to a rotational body with a radius of $0.075\ \mathrm{m}$. the corresponding position measurement resolution of the angle of the 1-DoF setup is $0.2\ \mathrm{nrad}$.

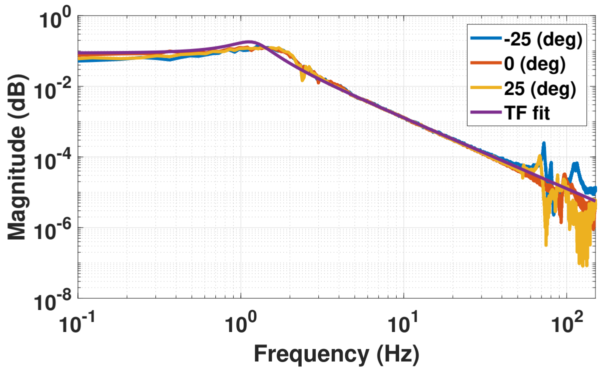

Fig. 3. The frequency response of the system measured at -25, 0, $250°$ with different responses.

The motor driver is set in the current mode control setting. Its current loop runs a PI controller with a crossover frequency of $65\ \mathrm{V\,A^{-1}}$ and a sampling frequency of $2-4\ \mathrm{kHz}$ [9]. The motor driver has a quantization on the output of $1\ \mathrm{mA_{RMS}}$, which turned out to be one of the key limiting factors for the accuracy together with the current noise of $4-9\ \mathrm{mA_{RMS}}$ produced by the motor driver[1]. Higher level control executed on a Simulink real-time platform at a sampling frequency of $1\ \mathrm{kHz}$.

The system's dynamic behaviour is identified using a chirp signal from 2 to $500\ \mathrm{Hz}$ with an amplitude of $50\ \mathrm{mA_{RMS}}$. This is energetic enough, such that the linear behaviour is visible. Moreover, the procedure was performed at various positions to illustrate the positions influence on the system's responce. The transfer function of the system was fitted manually to the response at $0°$ and is identified as

$$G(s) = \frac{1}{0.2s^2 + 0.74s + 11.46}, \tag{1}$$

which is a fully observable and controllable plant. The input is expressed in $\mathrm{mA_{RMS}}$ and the output in degrees. Fig. 3 shows the measured system response and the fitted transfer function. This transfer function is used for all the control designs and the simulations. The transfer function is accurate up to the second resonance frequency, which, depending on the position of the system, is between 65 to $80\ \mathrm{Hz}$. Furthermore, the system has a delay of 3 time steps.

Control Design

The lack of friction and a self-locking drive result in a situation where every disturbance on the system is measurable on the output. Furthermore, the stiffness of the flexures causes the system to be out of equilibrium during standstill. To meet the required repeatability of $50\ \mathrm{nm}$, a feedback controller is required to compensate the various disturbances on the system, such as input disturbance caused by the motor driver.

The control design is separated into two sections. First, the feedback controllers are designed to ensure the desired

[1] A more in-depth analysis of the current noise and its consequences is found in section C-B.

TABLE I
OVERVIEW OF THE COMPONENTS USED IN THE 1-DOF SYSTEM.

Component	Product name	Main specifications
Motor driver	Kollmorgon AKD-P00306 [9]	Continuous current of 3 $\mathrm{A_{RMS}}$, Peak current of 9 $\mathrm{A_{RMS}}$
Encoder	Heidenhain LIC-401 (411) [10]	Position resolution $\pm 2 \cdot 10^{-9}$ m
Motor	Tecnotion QTR-A-133-60-N [11]	Motor constant, K_m, of 5.57 $\mathrm{Nm/A_{RMS}}$, continuous current of 3.93 $\mathrm{A_{RMS}}$, peak current of 7.37 $\mathrm{A_{RMS}}$, and an ultimate 13.5 $\mathrm{A_{RMS}}$.
Controller	Speedgoat [12]	Quad core Intel Celeron, 4GB RAM memory, and 32GB SSD running Matworks Simulink Real-time with a sampling frequency of 1000 Hz

standstill performance and to cancel disturbances. Secondly, feedforward control is implemented for an increase in tracking performance.

Feedback

Four feedback controllers are chosen for their advantages. First, Proportional-Integral-Derivative control (PID) for its simplicity and its widespread use in industry [13]. Second, H_2 control for its optimality and minimalization in noise [14]. Third, Sliding Mode Control (SMC) and Super Twisted Sliding Mode Control (STSMC) for its robustness, model independence and tracking performance [15]. Finally, Linear and Non-Linear Active Disturbance Rejection Control (LADRC, NLADRC) for to its robustness, model independence and overall high performance [16].

PID Control

In 1922 N. Minorsky introduced the PID [17] and although it is the oldest feedback controller, it is still the most commonly used feedback controller in industry, mainly due to its simplicity and robustness against parameter changes [13]. The continuous PID controller in parallel form is given by

$$K(s) = K_\mathrm{p} + \frac{K_\mathrm{i}}{s} + \frac{K_\mathrm{d} s}{s\tau + 1}, \tag{2}$$

where K_p, K_i, and K_d are the proportional, integral and derivative gains respectively. τ is the time constant selected a priori which limits the high-frequency gain of the PID-controller [18]. The process of designing a controller which has a high performance and stability is relatively complex. Due to its parallel nature, each parameter has to be individually tuned. An indication of its complexity are the more than 8.000 hits on www.scopus.com when one searches for ”PID” and ”tuning”. Van Dijk et al. [18] proposed a tuning method for a serial PID-controller, which reduces the amount of tuning parameters and has a much clearer connection to the tuning process. The main idea behind the method is to have maximum phase lead at the open-loop cross-over frequency ω_c to ensure stability. The method maintains the characteristics of a PID controller such as the high gain at low frequencies. For a (dominant) second-order system with equivalent mass m_eq, the serial PID controller is described by

$$K(s) = k_\mathrm{p} \cdot \frac{(s\tau_\mathrm{z} + 1)(s\tau_\mathrm{i} + 1)}{s\tau_\mathrm{i}(s\tau_\mathrm{p} + 1)}, \tag{3}$$

where τ_p, τ_z, τ_i, and K_p are defined by ω_c, α, and β through the following relationships

$$\begin{aligned} \tau_\mathrm{z} &= \frac{\sqrt{\frac{1}{\alpha}}}{\omega_\mathrm{c}}, & \tau_\mathrm{i} &= \beta \cdot \tau_\mathrm{z}, \\ \tau_\mathrm{p} &= \frac{1}{\omega_\mathrm{c} \cdot \sqrt{\frac{1}{\alpha}}}, & k_\mathrm{p} &= \frac{m_\mathrm{eq}\omega_\mathrm{c}^2}{\sqrt{\frac{1}{\alpha}}}. \end{aligned} \tag{4}$$

Here, the parameter ω_c defines the cross-over frequency at which the phase lead is designed to reach its maximum. The parameter α defines the amount of phase-lead by placing the poles closer or further away of the cross-over frequency and is usually set between 0.1 and 0.3. The parameter β ensures that the phase-lag of the integrator does not interfere with the phase lead of the derivative action by positioning the integrator pole further below the pole of the derivative, therefore, $\beta > 1$. The last parameter, k_p, scales the controller with the system's inertia.

Knowing the design and the identified system, the PID controller can be designed using Eq. (1). To reduce noise sensitivity, the bandwidth of the controller is set as high as possible. The limit on the bandwidth is found to be an ω_c of 35 Hz, with α equal to 0.1, and β equal to 2. The delay in combination with the sample frequencies limits the crossover frequency. The open-loop response of the designed PID controller is shown in Fig. 4 from which can be seen that stability up to 35 Hz is obtained and that the system's noise sensitivity is reduced. Analysis shows a bandwidth of 60 Hz. The process sensitivity is shown in Fig. 6.

H_2 Control

The first commonly used alternative to the PID presented here is the H_2 control design. H_2 control its goal is to minimize the overall energy transfer in the system, which results in a minimal noise sensitivity and therefore, the best standstill performance. It was developed in the 1980s and is the result of the robust control philosophy. The H_2 control design used here is adapted from Kwakernaak [14]. It is commenly called a ”mixed sensitivity” problem, which minimizes the energy in the frequency domain and by Parseval's equality also in the time domain.

Its solution is optimized by adding weights to the system, emphasising the location of minimalization. W_1 is the weight on the output and W_2 is the weight on the input. Both of these weights are important in different frequency regimes.

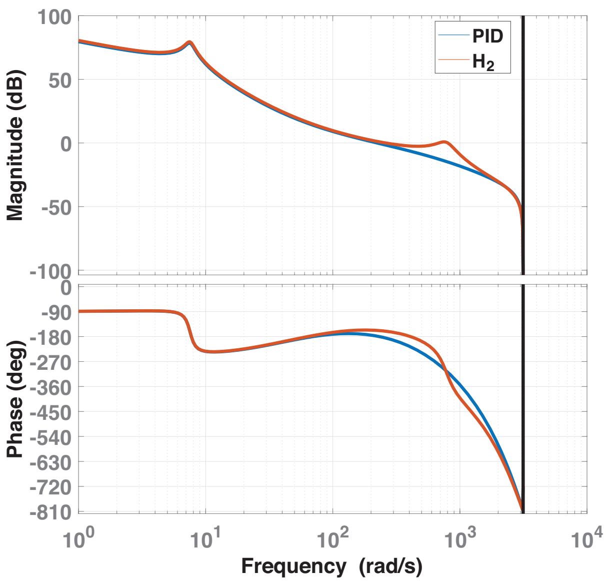

Fig. 4. Open loop response for PID and H_2 control. The black line is placed at 500 Hz and relates to the nyquist frequency.

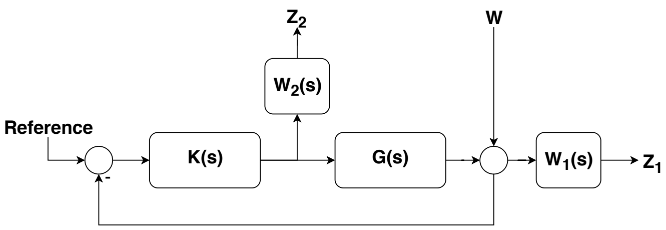

Fig. 5. Schematic of the H_2 controller. The positions of W1 and W2 indicate the signal used for the algorithm.

W_1 is dominant in the lower frequency regime and W_2 at higher frequencies. The overall layout of the system with the controller is shown in Fig. 5. The control problem can be solved by minimizing the following L_2 norm:

$$\begin{aligned} &||\,[W_1 S, W_2 KS]\,||_{H_2}^2 = ||W_1 S||^2 + ||W_2 KS||^2 \\ &= \frac{1}{\pi}\int_0^\infty |W_1(i\omega)S|^2 + |W_2(i\omega)K(i\omega)S(i\omega)|^2 d\omega, \end{aligned} \tag{5}$$

where K is the controller and S the sensitivity function which is $S = \frac{1}{1+gk}$. The optimal controller for the system minimizes this L_2-norm and therefore tries to keep both $|W_1 S|^2$ and $|W_2 KS|^2$ as small as possible. To have zero steady-state error, an integral action is required. This is done by adding an integrator (s^{-1}) to W_1, which results in the sensitivity function being small in the low-frequency range. The integral action has to be cut off after a certain frequency, since otherwise, its phase lag would negatively influence the system. So, the cutoff frequency is chosen to be equal to the PID controller, which is at 30 Hz. Furthermore, it is known that the current noise at the input is the dominant disturbance. So, by adding the plant, P, to W_1, the input sensitivity of the system is reduced. W_2 mainly influences the amplitude of the input. Attaching importance to its amplitude does not result in better noise rejection. Therefore its size is kept much smaller than the size of W_1 such that the minimalization of W_1 becomes dominant. Concluding, the following weights are chosen:

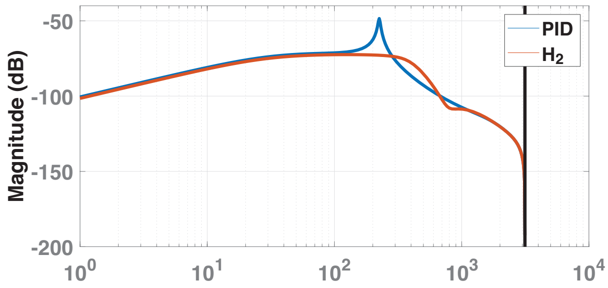

Fig. 6. Process senstivity of PID and H_2 control.

$$\begin{aligned} W_1(s) &= \alpha\frac{G(s)\cdot(s+30)}{s}, \\ W_2(s) &= 1e^{-8}. \end{aligned} \tag{6}$$

The variable α is added as a scalings factor chosen to be equal to 10. Based on the weights, the controller is calculated using the Matlab command *h2syn*. The resulting controller is of 5^{th} order, as expected, due to the added orders by the weights [14] and has a bandwidth of 70 Hz. The open-loop response of the resulting controller is shown in Fig. 4 and the sensitivity in Fig. 6. Its shape has the same characteristics as an PID-plus where an aditional phase is added in the higher frequency region to increase the bandwidth.

Sliding Mode Control

Sliding Mode Control (SMC) is a well-known discontinuous feedback control technique. Its design originates from the Soviet Union around the 1950s. The first western publication is done by Itkis in 1976 [19]. Its strength is in handling bounded uncertainties, disturbances, and parasitic dynamics due to its non-linearity [15]. The SMC algorithm design entails two phases, namely, design of the sliding mode surface, σ, and design of the control input. The sliding mode surface defines the dynamics over which the error is minimized. A typical sliding surface, which is also used for the system, is

$$\sigma = \left(\frac{d}{dt} + p\right)^k \cdot e. \tag{7}$$

The parameter e is the error between the reference, r and the output, y. The goal is to control the variable σ to zero. The choice of the positive parameter p is tuneable and defines the unique pole of the resulting "reduced dynamics" during sliding. The parameter k, however, is critical and has to be equal to $r-1$ with r being the relative degree between y and u, which is 2 for the plant. The second phase defines the control input, u, as a function of σ. The standard version of the control input is

$$u = -K\text{sign}(\sigma). \tag{8}$$

The input changes on the sign of σ and the variable K indicates its amplitude. During its reaching phase, the control variable u is constant, however, in steady state u commutes at a very high (theoretically infinite) frequency between the values $u = K$ and $u = -K$. This switching between the positive and negative value is known as chattering, which is a drawback of the standard sliding mode control. The amplitude and speed of the chattering depend on both the delay and sample frequency [15]. The influence of chattering on our plant is more extensive than for conventional systems due to the lack of friction, which makes any chattering measurable. This, together with the high-performance requirement, makes that the standard SMC does not yield satisfying results. Neither does the usual solutions such as a smoothing function as described in [20].

An alternative to the earlier proposed control input function is a second order sliding mode control, a so-called Super Twisting Sliding Mode Control (STSMC). This makes the control signal continuous in time while maintaining its performance and its ability to converge in finite time [20]. The STSMC uses the same sliding surface as the normal SMC but with a different control action

$$\begin{aligned} u &= -\lambda\sqrt{|\sigma|}\text{sign}(\sigma) + w, \\ \dot{w} &= -W\text{sign}(\sigma), \end{aligned} \tag{9}$$

with the parameters U and W defined as

$$\lambda = \sqrt{U}, \quad W = 1.1U, \tag{10}$$

where U is a positive constant which is taken sufficiently large. The result can be described as a non-linear PI controller, which yields a continuous input signal due to the integral action. This solves the chattering issue and no longer attenuates the high-frequency components. Furthermore, it yields better standstill performance. However, it also compromises the response time due to the integral action. The system is found to behave optimally for an U equal to 1000. This yields a response, which is neither too strong that it would reintroduces chattering, nor so weak that it would no longer filters the disturbances. The STSMC yields a decrease in disturbance rejection but a better standstill performance than the standard SMC due to the reduction of chattering.

Active Disturbance Rejection Control

Active Disturbance rejection control (ADRC) is the newest of the four compared feedback controllers. It was originally presented by Han in 1999 in Chinese and in 2009 in English [16]. It was presented as the next step in control engineering, which would replace PID in the industry. Some examples of application in industry are discussed in [21], [22], [13] with beneficiary results. It strives to address four weaknesses of PID: First, computational errors. Second, noise degradation in the derivative control. Third, oversimplification and the loss of performance in the control law in the form of a linear weighted sum. And finally, the complications brought by the integral control [16]. ADRC is based on the formulation of state feedback control and heavily relies on the Extended State Observer (ESO) for the improvements over PID, which yields the improved disturbance rejection property and integral behaviour. Additionally, the ADRC is composed of a convergence technique based on either a linear or a nonlinear function, which are applied to the observer and controller gains [16]. Furthermore, a Transient Profile Generator (TPG) generates a smooth control reference. The topology of the ADRC framework is shown in Fig. 7. ADRC, similar to PID, is a non-model-based control strategy which requires minimal information of the plant, requiring only the knowledge of the plant's inertia and the sampling time.

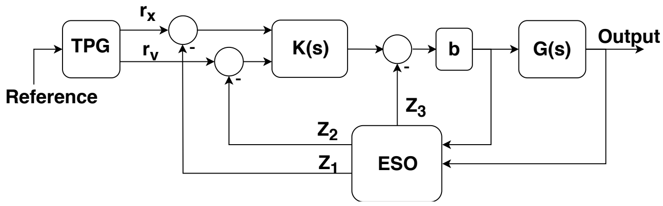

Fig. 7. The ADRC topology with the individual components.

The ADRC framework here is applied on a second order SISO plant to show its potential. However, the framework can also be applied to first and higher order plant, which can also be MIMO [13]. The second order plant is described by

$$\begin{aligned} \dot{x}_1 &= x_2, \\ \dot{x}_2 &= f(x_1, x_2, w(t), t) + bu, \\ y &= x_1, \end{aligned} \tag{11}$$

where u is the system's input, y is the system's output, b is either a linear function or a bounded non-linear function, and $f(x_1, x_2, w(t), t)$ is a bounded non-linear function that contains terms of the state vector x, which can be seen as the internal disturbances since the plant dynamics do not match the plant's model, external disturbances $w(t)$, and time t. From this formulation of the plant, the features of the ADRC can be designed. Firstly, the transient profile generator (TPG) is designed. Secondly, the extended state observer (ESO) is presented. Lastly, the linear or nonlinear feedback parameters are constructed.

Transient Profile Generator

The transient profile generator proposed by Han [16] is obtained by a time-optimal solution for the control of a double integrator plant. His primary motivation for the TPG is to filter setpoint jumps in the reference so that the reference signal becomes more suitable for tracking. Its result is an input signal which contains less energy in the higher frequencies, and, therefore, reduces the tracking error. Furthermore, it improves the settling time. The TGP is formulated as

$$\begin{aligned} \dot{v}_1 &= v_2, \\ \dot{v}_2 &= -r\text{sign}\left(v_1 - v + \frac{v_2|v_2|}{2r}\right), \end{aligned} \tag{12}$$

where v is the desired value of x_1, v_1 is the desired trajectory and v_2 the derivative of v_1. Where as the parameter r is used to limit the acceleration of the transient profile. The proposed solution, however, could introduce significant numerical errors in a discrete-time implementation. Therefore, a discrete-time solution is designed as

$$\begin{aligned} v_1 &= v_1 + hv_2, \\ v_2 &= v_2 + hu, |u| \leq r, \end{aligned} \tag{13}$$

where $u = F_{\text{han}}(v_1, v_2, r_0, h_0)$. The function F_{han} limites the accelerations. It is described by

$$\begin{aligned} d &= h_0^2 r_0, \\ a_0 &= h_0 v_2, \\ y &= v_1 + a_0, \\ a_1 &= \sqrt{d\left(d + 8|y|\right)}, \\ a_2 &= a_0 + \text{sign}\left(y\right) \cdot \frac{a_1 - d}{2}, \\ s_y &= \frac{\left(\text{sign}\left(y+d\right) - \text{sign}\left(y-d\right)\right)}{2}, \\ a &= \left(a_0 + y - a_2\right) s_y + a_2, \\ s_a &= \frac{\left(\text{sign}(a+d) - \text{sign}(a-d)\right)}{2} \\ F_{\text{han}} &= -r_0 \left(\frac{a}{d} - \text{sign}(a)\right) s_a - r_0 \text{sign}(a). \end{aligned} \tag{14}$$

The function F_{han} guarantees the fastest convergence from v_1 to v without an overshoot. The parameters r_0 and h_0 are equal to r and the sample time h, which can be tuned for the desired speed and smoothness. It is important to remark that this equation is different than the version presented by Han[16]. The author found that the version in Han's paper contains $d = h_0 r_0^2$, which caused unstable results.

Extended State Observer

Next, the Extended State Observer (ESO) of the framework is described. The ESO is used to estimate the disturbance on the plant compared to a plant in output canonical form. The use of a plant in canonical form for the observer eliminates the requirement of a mathematical expression for the actual plant which makes it much easier to use compared to other observers while maintaining a high performance [23]. An ESO is applicable for most nonlinear MIMO time-varying systems, but will here be applied to the second order SISO system described earlier in Eq. (1).

The objective is to make the output, y, behave as desired using u as the manipulative variable. To accomplish this the ESO treats the disturbance, $f(x_1, x_2, w, t)$, as an additional state, x_3. Let $\dot{f} = G(t)$. As mentioned earlier, f does not need to be known to be estimated, just like $G(t)$. The original plant is now described by

$$\begin{aligned} \dot{x}_1 &= x_2, \\ \dot{x}_2 &= x_3 + bu, \\ \dot{x}_3 &= G(t), \\ y &= x_1, \end{aligned} \tag{15}$$

which is always observable. The ESO can now be constructed as a state observer, which makes use of the additional state, in the continuous form of

$$\begin{aligned} e &= z_1 - y, \\ f_{\text{e}} &= f_{\text{al}}(e, \alpha_1, \sigma), \\ f_{\text{e1}} &= f_{\text{al}}(e, \alpha_2, \sigma), \\ \dot{z}_1 &= z_2 - \beta_1 e, \\ \dot{z}_2 &= z_3 + \frac{u}{b_0} - \beta_2 f_e, \\ \dot{z}_3 &= -\beta_3 f_{e1}. \end{aligned} \tag{16}$$

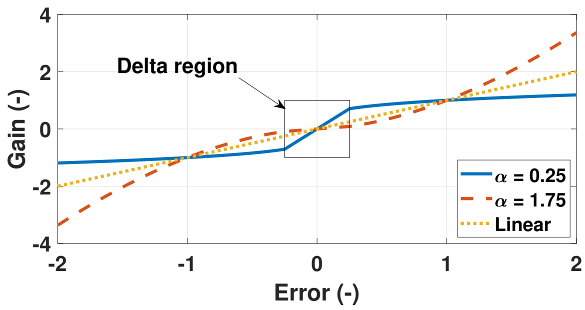

Fig. 8. Comparison of linear and nonlinear gains with variyng α for the function f_{al}. The inside of the delta region shows the region where the gains behave linear. Outside the delta region the gains are nonlinear.

A discrete implementation can be found in the paper of Han [16]. The ESO can be used with either linear or nonlinear gains. For the nonlinear ESO the functions f_e and f_{e1} are used to compute the nonlinear gains which rely on the function f_{al}:

$$f_{\text{al}} = \begin{cases} \frac{e}{\delta^{1-\alpha}}, & |x| \leq \delta \\ |e|^{\alpha}\text{sign}(e), & |x| > \delta \end{cases} \tag{17}$$

where δ indicates the linear gain region. An illustration of F_{al} is presented in Fig. 8. It shows that: $\alpha \geq 0$ tunes the nonlinear gains. $\alpha \leq 1$ results in a big gain within the δ region and small outside. $\alpha \geq 1$ results in a small gain within the δ region and big outside. For $\alpha = 1$, the result is a linear gain and $\alpha = 0$ results in a "bang-bang control" similar to SMC. This is illustrated in Fig. 8 where it is compared to a linear gain. The nonlinearity of the function f_{al} yields a remarkable improvement and results in convergence in finite time [16]. α_1 and α_2 are empirically determined to be equal to 0.25 and 0.3. The poles for the nonlinear ESO are

$$L_{\text{nonlin}} = [\beta_1, \beta_2, \beta_3]^T = \left[\frac{1}{0.3h}, \frac{2^2}{h\sqrt{h}}, \frac{5\sqrt{5}}{h^2}\right]. \tag{18}$$

These values of β_1, β_2, and β_3 have again been determined empirically. When one prefers to use a linear ESO then f_{e} and $fe1$ are replaced by e. The poles for the linear ESO are tuned as a function of ω_{o} and are described by

$$L_{\text{lin}} = [\beta_1, \beta_2, \beta_3]^T = \left[3\omega_o, 3\omega_o^2, \omega_o^3\right]^T. \tag{19}$$

The estimated disturbance by the extended state z_3, from either the nonlinear or linear ESO, can be used to cancel any disturbance measured. By applying the following control law

$$u = b_0 \left(-z_3 + u0\right), \tag{20}$$

the system can cancel both the internal disturbances and external disturbances. This control law reduces the overall system to

$$\ddot{y} = f - b_0 z_3 + b_0 u_0 \approx b_0 u_0, \tag{21}$$

which is a typical second-order integral plant. At this point, all the disturbances have been cancelled indeed without the need for a mathematical expression of f. A critical remark to make here is that all the estimates of ESO depend on the measured value of x_1. Hence, the quality of the position measurement greatly affects the performance of the ESO [16]. The resulting system can be easily controlled by making u_0 a function of the error, as discussed below.

Feedback Controller

The last part of the ADRC is the feedback controller. The feedback controller will be implemented on the resulting cascade plant from the ESO. Two options are designed, a linear and a nonlinear feedback controller. The advantage of nonlinear feedback is that the error can reach zero in finite time, whereas linear feedback is only able to reach zero in infinite time [16]. The nonlinear feedback proposed by Han [16] is

$$u_0 = F_{\text{han}}(e_1, e_2, r, h_1), \tag{22}$$

where F_{han} is the function earlier described for the TPG. e_1 is the error in position $v_1 - z_1$, e_2 is the error in velocity $v_2 - z_2$, the parameter r sets the acceleration limit, and h_1 is the precision coefficient which sets the aggresiveness of the controller which is a multiple of the sample time h. The function F_{han} can also be used as the feedback controller since it results in a time-optimal solution for a second-order plant, which closely resembles the real plant with the ESO. The result is a feedback controller which reduces the steady state error in such a manner that an integral control together with its pitfalls can be avoided and have zero steady-state error without an integral action as in PID.

In case a linear controller is preferred, a simple PD controller is sufficient to yield decent performance with zero steady-state error due to the ESO, e.g

$$u_0 = \gamma_1 e_1 + \gamma_2 e_2, \tag{23}$$

where the poles of γ can be tuned as a function of ω_c

$$[\gamma_1, \gamma_2]^T = [2\omega_c, \omega_c^2]^T. \tag{24}$$

Now all the individual components have been explained the complete controller can be put together. Both the linear and nonlinear controller are designed and tested. The parameters which are used in both linear and nonlinear are noted first. The systems inertia, b_0, is 0.2. The sample time is $1\ \mathrm{ms}$. The maximum acceleration is set to $500\ \mathrm{rad\,s^{-2}}$, which corresponds to 5 G at the end-effector. Next, the parameters of the linear controller are explained. The linear active disturbance rejection controller (LADRC) has the crossover frequency of the observer placed at 80 Hz. Any higher crossover frequency for the observer results in instability. This instability is the result of the delay in combination with the sampling frequency. The crossover of the observer also limits the crossover of the PD controller, which is generally placed 10 times as slow as the observer [16]. The optimal crossover for the PD controller was found to be 5 Hz.

Lastly, the parameters for the nonlinear active disturbance rejection controller (NLADRC) are designed as a function of the sample time, h. The only parameter which yet to be defined is h_1, which is set to $10\ \mathrm{ms}$. If h_1 would be chosen smaller, then the system would become unstable due to the delay of 3 ms.

In the experiments, the TPG is removed since a fourth order reference profile is applied, which removes the benefit of the TPG. In operations where only a setpoint is given, the TPG would yield a performance increase.

Feedforward

Due to the highly deterministic nature of the system, feedforward of the dynamics potentially yields a significant improvement in its tracking performance. The feedforward can be separated into four elements: the acceleration, gravity, stiffness, and, lastly, the cogging. These elements together have been found to contain all the information to move the system to the desired position. The complete feedforward is described by

$$I_{\text{ff}} = I_{\text{m}} + I_{\text{g}} + I_{\text{s}} + I_{\text{c}}. \tag{25}$$

The complete design of the feedforward of the system dynamics is without a velocity dependent component, since there are no elements that influence the system, due to the lack of friction, or they are not big enough to be off a measurable influence such as the air.

The feedforward for PID, H_2, and SMC can easily be implemented as an additional input. However, the implementation of feedforward for ADRC requires some changes. Its observer is based on a moving mass which does not have the position related dynamics. Therefore, the acceleration and the other feedforward components have to be separated, and only the acceleration related components have to be applied to the observer. The complete feedforward has to be applied to the system, which reduces the differences between the observer and system. First, the individual elements are described. After this, all the feedforward elements are estimated at once using nonlinear regression.

Acceleration Feedforward

The acceleration feedforward can be easily calculated from the required acceleration. The required torque for the accelerations is described by

$$I_{\text{m}} = \frac{J\alpha}{K_{\text{m}}}, \tag{26}$$

where I_{m} is the computed RMS current required for the acceleration. K_{m} is the motor constant. J is the inertia of the system, and α are the rotational accelerations, which are given by the reference profile.

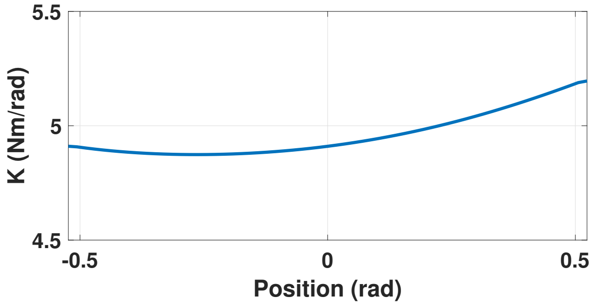

Fig. 9. The stiffness of the butterfly hinge mounted in the base over position.

Gravity Compensation

The gravity component depends on the system's position. The amount of torque required for compensating the gravitational forces on the system is

$$\tau_{\mathrm{g}} = \frac{mgl}{K_{\mathrm{m}}} \sin(2\pi \cdot \theta + \phi), \tag{27}$$

where m is the mass, which is $1.46\ \mathrm{kg}$, g is the gravitational constant, $9.813\ \mathrm{m\,s^{-2}}$, at the measurement location (Twente, Netherlands), l is the distance from the centre of rotation to the centre of the beam in meters. θ is the angle from the initial position, and ϕ is the initial position. The initial position is estimated using regression and is $3.6652\ \mathrm{rad}$ $(210°)$. [2]

Stiffness Feedforward

Simulations of the flexures show that a large and relatively linear stiffness can be expected. These simulation results are shown in Fig. 9 and indicate that the stiffness for a clockwise and counterclockwise rotation only has a minor difference of 5%. Therefore the assumption is made that both sides have a constant stiffness such that the stiffness can be estimated with a minimal amount of parameters, which is a linear function with an offset

$$I_s = \frac{a\theta + b}{K_{\mathrm{m}}}, \tag{28}$$

where a is the stiffness of the hinges and the variable b is due to the flexures not being in their neutral angle at $0\ \mathrm{rad}$.

Cogging Compensation

The cogging torque is a consequence of the permanent magnet synchronous motor (PMSM) and completely determined by the geometry [24]. It is the result of the interaction between the rotor's magnets and the iron in the stator which have a preferential position. This is where the reluctance is minimal [24]. If the PMSM is not at this preferential position, it experiences a torque towards this position. The cogging has zero mean over a full mechanical period and a periodicity matching with the motor design[3]. Furthermore, the cogging can be separated into a current independent and dependent element. For the feedforward design, the current dependent components are assumed to be negligible. This approximation is valid since the dependence only starts to play a role when the current rises above the maximum continuous current of $3\ \mathrm{A_{RMS}}$ [11].

The PMSM used in the setup has 21 poles and 28 magnets [11]. From this, the fundamental order of the waveform of the cogging can be calculated using the lowest common multiple of the poles and the magnets [25]. The resulting expected base harmonic, N_{b}, is $0.0748\ \mathrm{rad}$. The other components are a higher-order of this base harmonic. However, elements such as pivot shift of the flexure bearing (the displacement of the centre of rotation) or non-concentricity may cause cogging elements in frequencies other than the base or higher-order harmonics. Therefore, twenty sinusoids with estimated frequencies, amplitudes and phases are used

$$I_{\mathrm{c}} = \frac{1}{K_{\mathrm{m}}} \sum_{n=1}^{20} a_n \cos(b_n \theta + \phi_n), \tag{29}$$

with m being the number of sines used to fit the cogging, a_n the amplitude of that sinusoids, ϕ_n the estimated phase shift and b_n the estimated frequency.

Complete feedforward

Using the individual elements of the feedforward, the position related feedforward can be estimated at once. This minimizes the chance to misinterpret a component by other elements of the feedforward. Fig. 10 shows the reference current used for the estimation of the feedforward signal and the actual fit on the signal. The fit is made using a nonlinear estimation with Matlab with the initial values set to the values derived from a model of the system with nominal design parameters. The RMS error on the position related feedforward of the estimation is $1.93\ \mathrm{mA_{RMS}}$. By combining the fit shown in Fig. 10 with acceleration feedforward yields the complete feedforward which has been found to describe the system's dynamics.

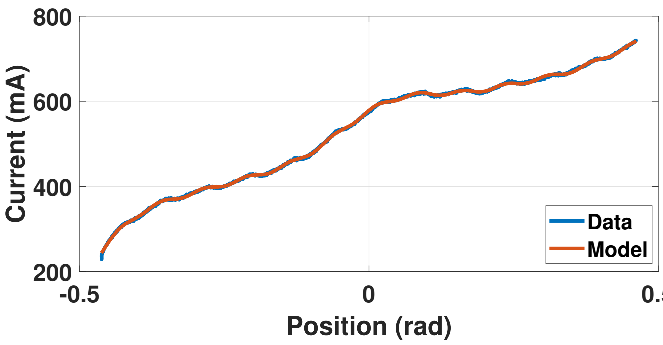

Fig. 10. The required current and estimated current for the feedforward over the position.

Experimental Results

The designed feedback controllers are compared on their performance at standstill position, tracking, and disturbance rejection. Standstill performance is the essential measure for the system. The expectation is that all controllers have their strengths and weaknesses, such as differences in standstill performance and tracking performance. The tracking performance

[2]See Appendix B for the full calculations.
[3]See section D for a full explenation regarding the cogging

is also evaluated in combination with feedforward, and it is expected that a more accurate feedforward will improve the tracking performance. The system's performance is evaluated with the RMS error and maximum error. For the disturbance tests the settling time is also displayed. The RMS error is calculated by

$$E_{\text{RMS}} = L\sqrt{\frac{1}{N}\sum_{n=1}^{N}(p_n - p_{\text{sp}})^2}, \tag{30}$$

where L is the transmision ratio of the complete system, N is the number of samples of the experiment, p_n is the measured position, and p_{sp} is the desired position. The overall results are shown in Table II.

Standstill performance

Position performance is potentially one of the unique specifications of the system, which has to be enabled by the feedback controller. Therefore, the feedback controllers are compared at the same position since the main goal of the system to minimize variance in the experiment.
It is tested by maintaining the same position for 160 s. No feedforward is used since the disturbances influencing the standstill performance are not implemented in the feedforward. Feedforward would, therefore, not result in different results. The results for the standstill RMS error are depicted in Fig. 11 and listed in Table II. In Fig.11 the cumulative power spectral density (CPSD) is shown, which illustrates the contribution of the frequency content of the noise spectrum to the RMS noise. It is calculated by the square root of the cumulative sum of the signal squared at each frequency. The final value of CPSD equals the RMS position error in Table II due to Parseval's identity.

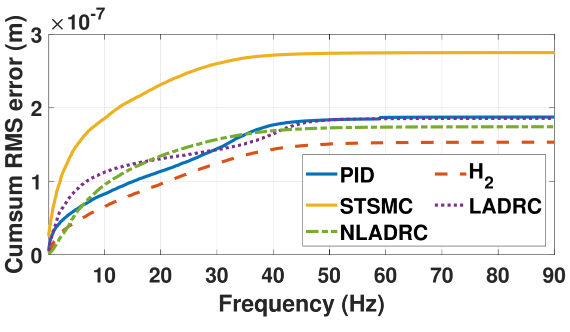

Fig. 11. Cumulative Power spectrum of the standstill error for various controllers.

The best performing controller is, as expected, the H_2 control. H_2 minimises the energy transfer in the system which should yield the best noise rejection characteristics. The result of PID closely resembles the shape of H_2. However, it is less effective in the lower frequency regime. This is expected since the open loop plot in Fig. 4 also shows a worse performance, which results in a higher noise level. The LADRC is made of two components, the PD controller and the ESO. Its PD controller has a relatively low crossover frequency, which results in a poor performance in this lower frequency region. The ESO, however, is its strong point and reduces the noise in the mid-frequency regime very efficiently. This induces that the overall noise level is identical to PID, although, with a different distribution. The NLADRC is tuned differently and has the best performance of all the controllers in the lower frequency regime. This is due to the nonlinearity of the controller, which allows it to be more aggressive. The STSMC has the highest RMS error of the controllers, which is the result of the integral action used to solve the chattering. The integral action causes a delay in the response and therefore, a higher noise level. Overall, the best performing controller is the H_2, which outperforms all the controllers in every frequency region beyond 3 Hz.

The system's standstill performance is limited by the amount of disturbance on the system. The main noise source is the motor driver, which exerts an RMS current noise of 4 mA_{RMS} in the current position. Furthermore, the motor driver has a quantisation on the current setpoint of 1 mA_{RMS}, which limits the performance of the system by making it impossible to cancel the disturbances with a smaller magnitude. The sampling frequency of 1 kHz together with the 3 time samples delay, places a limitation on the feedback controllers.

Tracking Performance

Although the main requirement on the feedback controllers is to achieve high standstill accuracy, the controllers can also be used for tracking a reference signal. Even though H_2 has the best standstill performance, the same does not have to be true for the tracking performance. To test this, all the feedback controllers have been tested for their performance in tracking a reference signal. The profile has to be sufficiently tough, such that the feedback controllers have difficulty tracking. Furthermore, it may not contain any discontinuities or other properties, which would make it physically impossible to track.

The reference profile is made following the method proposed by P. Lambrechts [26]. This creates a fourth order continuous reference profile. The reason that a fourth order motion profile is beneficial over, for example, a second order one, is that higher order trajectories inherently have a lower energy content at higher frequencies. This results in lower high-frequency content of the error signal, which in turn enables the feedback controller to be more effective [26], [18]. Therefore a finite jerk, acceleration, and velocity are required to reduce the tracking error [18].

Furthermore, higher order trajectories have less chance of demanding a motion which is physically impossible to perform by the motion system, for example, due to a 'rise time' in the current [26].
The designed motion has its initial position at -0.4363 rad ($-25°$) and ends at 0.4363 rad ($25°$), which corresponds to a stroke of 83% of the full range. The velocity is limited to $\pm 5/9\pi$ rad s^{-1} and the acceleration to $27/9\pi$ rad s^{-2}. The profile for one motion is depicted in Fig. 12. The profile is designed such that it uses almost the full range of the system with clearly distinguishable

TABLE II
OVERVIEW OF THE ERRORS OF THE VARIOUS CONTROLLERS FOR THE DIFFERENT EXPERIMENTS DONE.

	PID	H_2	STSMC	LADRC	NLADRC
Standstill RMS error (µm)	0.19	***0.16***	0.28	0.19	0.18
RMS error no feedforward (µm)	***174***	213	750	1957	545
Max. error no feedforward (µm)	***357***	489	2350	3674	1120
RMS error Acceleration feedforward (µm)	***153***	174	590	187	181
Max. error Acceleration feedforward (µm)	***374***	505	2295	492	481
RMS error Acceleration, gravity, and stiffness feedforward (µm)	***51.7***	86.7	67.0	76.1	87.1
Max. error Acceleration, gravity, and stiffness feedforward (µm)	***140***	225	203	200	200
RMS error Full feedforward (µm)	50.7	***43.6***	48.7	68.6	45.3
Max. error Full feedforward (µm)	145	***112***	174	222	123
Max. error step disturbance (µm)	137	166	14000	***131***	133
Settling time (ms)	255	305	374	245	***206***
Max. error sinusoidal disturbance (µm)	***8.8***	9.6	30.3	13.0	10.7

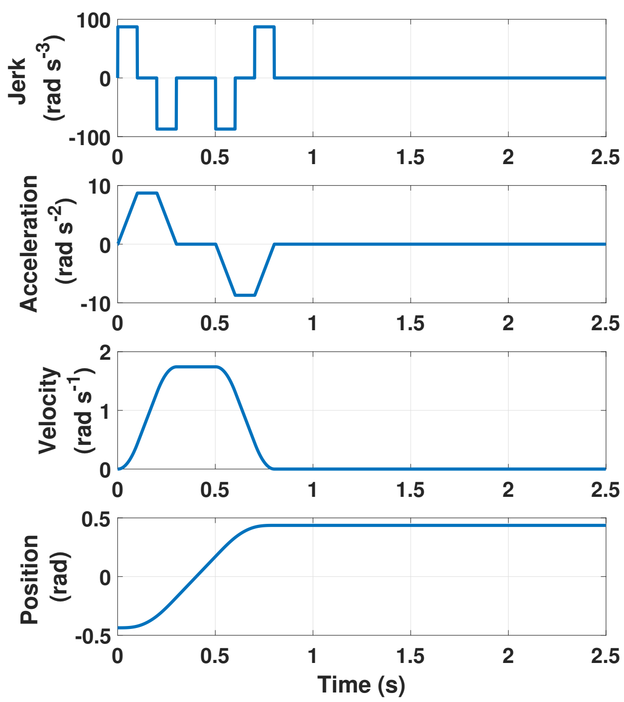

Fig. 12. The fourth order reference profile and its time derivatives as used for the tracking performance experiments.

sections of constant acceleration and velocity. Furthermore, the reference trajectory is within the specifications of the system.

This experiment has been extended by comparing the tracking performances with different levels of feedforward of the dynamical system components. The initial experiment is executed without feedforward. In subsequent experiments, feedforward components have been added to see their effect. The elements of the system's dynamics are added to the feedforward such that the amount of information required for the feedforward increases, in particular: no feedforward, acceleration feedforward, the addition of gravity and stiffness feedforward and addition of cogging. The controllers are evaluated on their performance in RMS error and maximum error during the reference trajectory.

The first test is carried out without any feedforward implemented. The error during this motion is shown in Fig 13 and the measures are listed in Table II as RMS and maximum error without feedforward. The LADRC has the largest error, which is highly dependent on the accelerations. This is the result of the low crossover frequency of the PD controller and the observer, as well as the system, being unable to track the reference profile. Therefore, the integral action performed by the observers is unable to function. However, during the constant velocity regime, the observer is able to perform its integral action, and the system's error becomes identical to the other controllers. Furthermore, its settling time is the largest, which is again due to the observer. The NLADRC shows similar results although its NL PD controller is more aggressive and therefore results in a smaller error related to the accelerations. This results in a smaller RMS error and settling time. The results of H_2 and PID are almost identical, which is predicted by their bode plots, which show a similar behaviour in the frequency regime at which this movement takes place. The STSMC lacks in performance due to the super twisting adaptation, which decreased its response time in favour of its standstill performance.

During the second experiment, the acceleration feedforward is added. The same reference trajectory is used to evaluate the performance. The results are shown in Fig. 14 and Table II for RMS and maximum error with acceleration feedforward. All the controllers show a decrease in RMS error during the accelerations phases. With a minimal improvement of the RMS

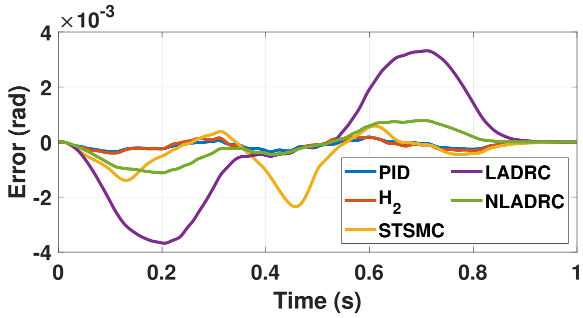

Fig. 13. The tracking error over time for the various controllers without feedforward.

error for PID, H_2, and TSMC since these already performed well during this phase. However, both LADRC and NLADRC show a significant improvement. This improvement origniates from the observer being able to better tracking the reference signal during this phase of the motion, which enables the disturbance rejection on the plant. The controllers, except for STSMC, now perform almost identical. The acceleration feedforward increases the performance of the system while it does not require any additional knowledge of the system than required for the design of PID, ADRC of STSMC, which makes it easy to implement.

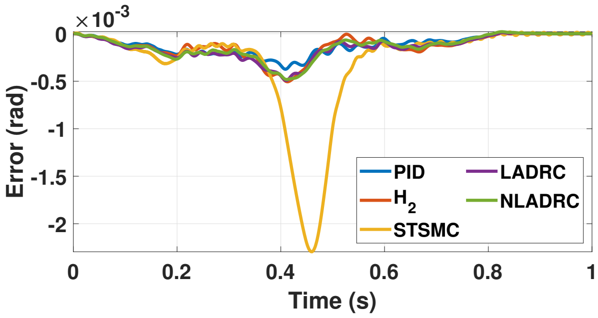

Fig. 14. The tracking error over time for the various controllers with acceleration feedforward.

The next elements added to the feedforward are gravity and stiffness. The gravity is a relatively constant torque over the workspace but does induce a big load on the systems. The stiffness is equal in magnitude, but the torque does change sign during the motion, which has a significant influence on the controllers. The load for controllers by adding these feedforward elements is, therefore, decreased significantly, as expected by a low-frequency approximation of the tracking error in [18]. The results are shown in Fig. 15 and Table II for RMS and maximum error with acceleration, gravity, and stiffness feedforward. All controllers show a significant improvement in their performance due to the addition in the feedforward. The performance of all the controllers is now almost within the same band with PID having the best overall performance. The remaining error is mainly due to the cogging, which is not implemented in the current feedforward. The cogging has a high variation, and, therefore, also has a high frequency content. The feedback controllers have a lower bandwidth, which makes them less successful to compensate

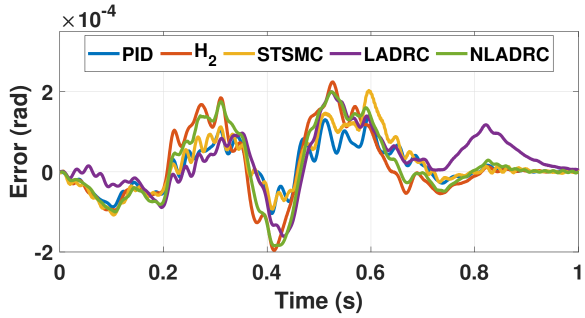

Fig. 15. The tracking error over time for the various controllers with acceleration, gravity and stiffness feedforward.

the coggin.

For the last experiment, cogging is added to the feedforward resulting in all known system dynamics being compensated. The results are shown in Fig. 16 and Table II for RMS and maximum error with full feedforward. This experiment resulted in the lowest RMS and max error. The results show that H_2 has the lowest RMS and max error with NLADRC being a close second. The remaining disturbances are high-frequent and therefore require high bandwidth to be compensated. The bandwidth of H_2 and NLADRC are higher than PID and therefore, yield a better result. However, the other controllers have an almost identical performance, which indicates that the feedforward cancels the system's dynamics well. The remaining error can be attributed to the feedforward not being an exact match with the disturbances due to the temperature dependence of the cogging or the quantisation of the current. This limits the resolution of the current, which, therefore, limits the resolution of feedforward and the feedback. The current required for compensating the remaining error is close to the quantisation limits. This makes further improvements difficult with the same setup.

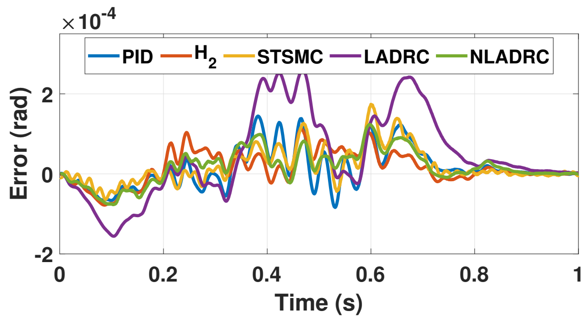

Fig. 16. The tracking error over time for the various controllers with full feedforward.

Overall, the best performer in terms of tracking performance is the H_2, yielding an RMS tracking error of $43.6\ \mu\text{m}$, when all the known system's dynamics are implemented in the feedforward. The RMS error is still a factor 400 larger than the standstill performance. When less information is used, the PID has the best performance. However, the performance differences are not significant. An interesting remark is that the non-linearity of the NLADRC did result in a performance increase over LADRC, which may be the result of the highly deterministic nature of the system. Furthermore, hysteresis in the current sensor, which has not been implemented in the feedforward, caused a significant part of the remaining error.

Disturbance Rejection

Another important aspect of the controllers is their performance in disturbance rejection. This is tested by injecting at $t = 0.25$ s a step disturbance of 200 $\mathrm{mA_{RMS}}$ for 0.4 s into the process. This results in an angular impulse of $0.22\mathrm{N\,m\,s}$.
The results are shown in Fig. 17 and Table II. The STSMC has the largest maximum error as a result of the disturbance, which is expected since its response is slower due to the integral action used to remove the chattering. The other controllers have an almost identical maximum error with the LADRC performing the best response overall. That the ADRCs have the best response can be explained by the fact that the error caused by a step disturbance is compensated by the ESO, which has a higher bandwidth than the integrators of PID and H_2. For the same reason, the ADRCs also have the fastest settling time. Furthermore, PID and H_2 have a small phase margin resulting in oscillations while reaching steady state, whereas the NLADRC does not have these oscillations due to the higher bandwidth resulting from the non-linearity.

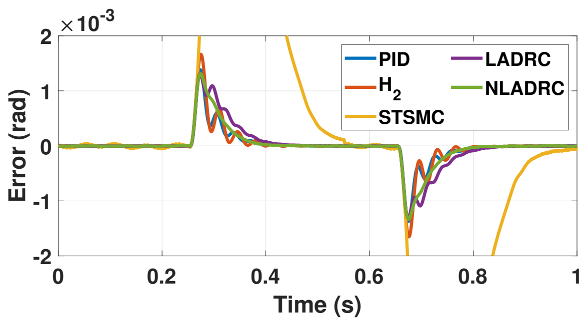

Fig. 17. The systems response with different controllers to a step disturbance 200 $\mathrm{mA_{RMS}}$ applied from 0.25 s untill 0.65 s.

Next, a sinusoidal disturbance is added. A sinusoid of 50 $\mathrm{mA_{RMS}}$ and 2 Hz is injected to the system. The 50 $\mathrm{mA_{RMS}}$ causes a torque of 0.28 $\mathrm{N\,m}$. The frequency of 2 Hz is chosen such that it is well within the bandwidth of all the controllers. The performance of the feedback controllers is measured by the maximum error of the system.
The results are shown in Fig. 18 and Table II. For a sinusoidal disturbance, the PID controller has the best performance, and the performances of H_2 and NLADRC are only slightly worse. The STSMC, again, falls behind the other controllers.

Evaluation and Recommendations

For the design goal of finding the best feedback controller for standstill performance, H_2 control yielded the best results. The higher bandwidth of H_2 compared to PID results in a better disturbance rejection and therefore, a better standstill performance. NLADRC's standstill performance was slightly

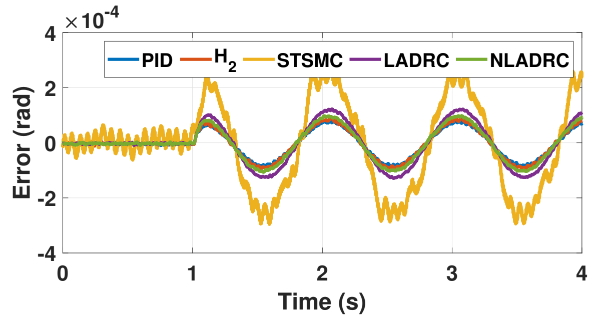

Fig. 18. The systems response for a sinusoidal disturbance of 50 $\mathrm{mA_{RMS}}$ for the different feedback controllers.

better than PID, however behind on H_2. The STSMC had the worst standstill performance of the feedback controllers, which is related to the integral action, which increases its response time. Therefore, it can be concluded that for a standstill task on the considered system, STSMC is not an appropriate algorithm, but it did show a decent tracking performance. The difference in PID and LADRC found in [8] is found to be mainly caused by the TPG. The performances here was much more identical since a smooth reference profile was chosen, which removed the advantage of the TPG.

Overall the desired standstill performance of 50 nm has not been achieved with the current setup. However, no mechanical influences were found to limit performance. Several measures can be taken to achieve the 50 nm. The current noise can be reduced by changing the motor driver. The effect of current noise can be reduced by decreasing the motor constant or increasing the inertia, however, it comes at the cost of a decreased maximum acceleration. Finally, suppression of the current noise can be improved by increasing the sampling frequency or decreasing the delay, allowing for a higher crossover frequency. An experiment using H_2 on a sample rate of 4 kHz resulted in a standstill performance of 106 nm. Furthermore, it is considered to double the inertia, which would result in 53 nm, being close to the objective. Using the additional inertia to balance gravity effects and (partly) joint stiffness makes sure that the maximum acceleration is not affected too much.

The tracking performance showed a more significant difference across the different controllers, especially when the feedforward is not implemented. Without the feedforward, the performance of STSMC, LADRC, and NLADRC is at least a factor 2 below the H_2. Each additional of the system dynamics increased the tracking performance significantly. However, the tracking error with full feedforward implemented remained a factor 400 above the standstill error. Of the compared controllers, H_2 control has the best tracking performance of the compared controllers, which follows from the higher bandwidth.

The best controller for a step disturbance rejection was found to be either the LADRC or the NLADRC, which is contributed to the ESO. For a sinusoidal disturbance, the PID has the best rejection.

CONCLUSION

Four feedback control algorithms have been compared for their standstill performance for a flexure-based system without friction or a self-locking drive. Such an extensive comparison of these four feedback controllers (PID, H_2, STSMC, and ADRC) has not yet been found in the literature. Filling this gap highlights the properties of the various controllers and allows practitioners to choose an appropriate feedback controller for their task.

The optimal controller for standstill performance was found to be the H_2 control due to the highest bandwidth, while PID, LADRC and NLADRC had an almost identical performance. STSMC performed below the bar and should not be chosen for a standstill task. The tracking performance of different feedback controllers has also been compared with again H_2 yielding the best performance when the feedforward cancels all low-frequency components. When no feedforward is used, PID resulted in the best results. For the disturbance rejection PID, H_2, and both ADRC's yielded similar results with NLADRC having the fastest settling time.

Overall, the best control method for the considered control problem is the H_2 control.

The required standstill performance has not been realised, but the work provided insights for modifications on the mechanics and electronics to achieve the specification.

ACKNOWLEDGMENT

The author would like to thank the following companies for their support and technical advice for this project; Tecnotion B.V., Almelo, The Netherlands; Heidenhain Netherlands B.V., Ede, The Netherlands; SigmaControl B.V., Barendrecht, The Netherlands. Futhermore, the author would like to thank; Dr. Ir. W. B. Hakvoort, Ir. M. Naves, Ir K. H. R. Rouwenshorst, Dr. Ir. T. L. van Vuure and everyone else who contributed to this article.

REFERENCES

[1] DH Wiersma, SE Boer, Ronald GKM Aarts, and Dannis Michel Brouwer. Design and performance optimization of large stroke spatial flexures. *Journal of Computational and Nonlinear Dynamics*, 9(1):011016, 2014.

[2] M. Naves, R.G.K.M. Aarts, and D.M. Brouwer. Large stroke three degree-of-freedom spherical flexure joint. pages 97–98, 2017. cited By 2.

[3] Naves M. D. W. Vogel D. M. Brouwer Hakvoort, W.B.J. Mechatronic design of a flexure based 6rss parallel robot. 2019.

[4] Nicolas Pyschny. *Auslegung und Optimierung von festkörpergelenkbasierten Parallelkinematiken für die Montage von optischen Komponenten*. Apprimus-Verlag, 2014.

[5] S. Chillari, S. Guccione, and G. Muscato. An experimental comparison between several pneumatic position control methods. In *Proceedings of the 40th IEEE Conference on Decision and Control (Cat. No.01CH37228)*, volume 2, pages 1168–1173 vol.2, Dec 2001.

[6] Wen-Bin Lin and Huann-Keng Chiang. Super-twisting algorithm second-order sliding mode control for a synchronous reluctance motor speed drive. *Mathematical Problems in Engineering*, 2013, 2013.

[7] Arkadiusz Mystkowski. The robust control of magnetic bearings for rotating machinery. *Solid State Phenomena*, 113:125–130, 01 2006.

[8] Gernot Herbst. A simulative study on active disturbance rejection control (adrc) as a control tool for practitioners. *Electronics*, 2(3):246–279, 2013.

[9] Kollmorgenn. *Data sheet for akd-xzzz06-0069*, 2017 (accessed June 2, 2019). https://www.kollmorgen.com.

[10] Kollmorgenn. *Datasheet for exposed linear encoder LIC-401 (411)*, 2017 (accessed June 2, 2019). https://www.heidenhain.nl.

[11] Tecnotion. *Frameless torque motor series*, 2018 (accessed June 2, 2019). https://www.tecnotion.com.

[12] Speedgoat. *Datasheet for Baseline real-time target machine - S*, 2019 (accessed June 2, 2019). https://www.speedgoat.com/products-services/real-time-target-machines/baseline.

[13] Qing Zheng and Zhiqiang Gao. On practical applications of active disturbance rejection control. In *Proceedings of the 29th Chinese control conference*, pages 6095–6100. IEEE, 2010.

[14] Huibert Kwakernaak. H2-optimization — theory and applications to robust control design. *Annual Reviews in Control*, 26(1):45 – 56, 2002.

[15] Christopher Edwards and Sarah Spurgeon. *Sliding mode control: theory and applications*. Crc Press, 1998.

[16] Wen-Hua Chen, Jun Yang, Lei Guo, and Shihua Li. Disturbance-observer-based control and related methods—an overview. *IEEE Transactions on Industrial Electronics*, 63(2):1083–1095, 2016.

[17] Nicolas Minorsky. Directional stability of automatically steered bodies. *Journal of the American Society for Naval Engineers*, 34(2):280–309, 1922.

[18] Johannes Van Dijk and Ronald Aarts. Analytical one parameter method for pid motion controller settings. *IFAC Proceedings Volumes*, 45(3):223–228, 2012.

[19] Uri Itkis. *Control systems of variable structure*. Halsted Press, 1976.

[20] Yuri Shtessel, Christopher Edwards, Leonid Fridman, and Arie Levant. *Sliding mode control and observation*. Springer, 2014.

[21] Li Sun, Donghai Li, Kangtao Hu, Kwang Y Lee, and Fengping Pan. On tuning and practical implementation of active disturbance rejection controller: a case study from a regenerative heater in a 1000 mw power plant. *Industrial & Engineering Chemistry Research*, 55(23):6686–6695, 2016.

[22] Qinling Zheng and Zhan Ping. Active disturbance rejection control for server thermal management. In *2018 5th International Conference on Control, Decision and Information Technologies (CoDIT)*, pages 158–163. IEEE, 2018.

[23] Zhiqiang Gao. Active disturbance rejection control: a paradigm shift in feedback control system design. In *2006 American control conference*, pages 7–pp. IEEE, 2006.

[24] Marián Tárník and Ján Murgaš. Additional adaptive controller for mutual torque ripple minimization in pmsm drive systems. *IFAC Proceedings Volumes*, 44(1):4119–4124, 2011.

[25] ZQ Zhu and David Howe. Influence of design parameters on cogging torque in permanent magnet machines. *IEEE Transactions on energy conversion*, 15(4):407–412, 2000.

[26] Paul Lambrechts. Trajectory planing and feedforward design for electromechanical motion systems. 2003-18, 2003.

[27] G Grandi and J Loncarski. Evaluation of current ripple amplitude in three-phase pwm voltage source inverters. In *2013 International Conference-Workshop Compatibility And Power Electronics*, pages 156–161. IEEE, 2013.

[28] LEM. *Data sheet for LTSR 15-NP*, 2017 (accessed June 4, 2019). https://www.lem.com/sites/default/files/products_datasheets/ltsr_15-np.pdf.

[29] Vishay. *Datasheet for vs-gt120da65*, 2017 (accessed June 2, 2019). https://www.vishay.com/docs/95737/vs-gt120da65u.pdf.

[30] Mohammad S Islam, Sayeed Mir, and Tomy Sebastian. Issues in reducing the cogging torque of mass-produced permanent-magnet brushless dc motor. *IEEE Transactions on Industry Applications*, 40(3):813–820, 2004.

[31] Bojan Grcar, Peter Cafuta, Gorazd Stumberger, and Aleksandar M Stankovic. Pulsating torque reduction for permanent magnet ac motors. In *Proceedings of the 2001 IEEE International Conference on Control Applications (CCA'01)(Cat. No. 01CH37204)*, pages 288–293. IEEE, 2001.

[32] COMSOL AB. Comsol multiphysics v. 5.2.

[33] Mark Thiele. *Analysis of cogging torque due to manufacturing variations in fractional pitch permanent magnet synchronous machines*. PhD thesis.

[34] Andrej Černigoj, Lovrenc Gašparin, and Rastko Fišer. Native and additional cogging torque components of pm synchronous motors—evaluation and reduction. *Automatika*, 51(2):157–165, 2010.

[35] Lovrenc Gašparin, Andrej Černigoj, and Rastko Fišer. Phenomena of additional cogging torque components influenced by stator lamination stacking methods in pm motors. *COMPEL-The international journal for computation and mathematics in electrical and electronic engineering*, 28(3):682–690, 2009.

APPENDIX A
SYSTEM IDENTIFICATION

The system's dynamic behaviour is identified using a chirp signal with a frequency from 2 to $500\ \mathrm{Hz}$. This is energetic enough, such that the linear behaviour is visible. The chirp is repeated eight times, which is averaged to reduce the amount of noise on the measurement. These experiments are carried out for the entire range of motion since it is expected that the system's response is position dependent due to the flexures. The position-dependent stiffness of these flexures results in position-dependent resonance frequencies. The response in time domain at $0\ \mathrm{rad}$ is shown in Fig. 19.

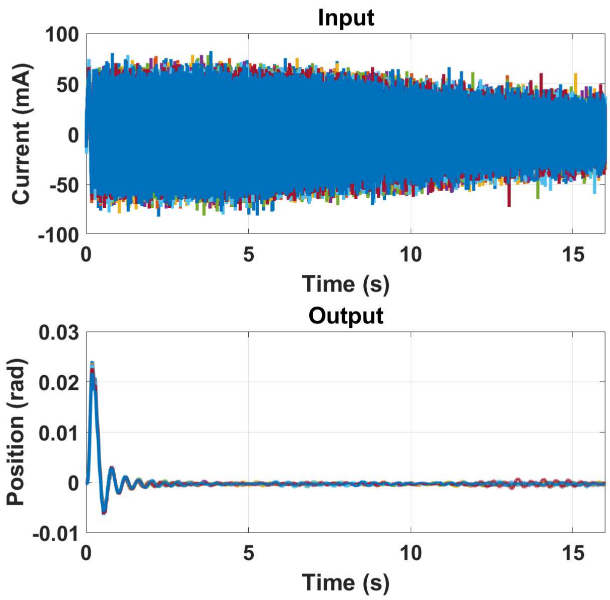

Fig. 19. Input and output signal in the time domain for eight chirps plotted over one another.

The responses in frequency domain for the entire range of motion can be found in Fig. 20. The variations in the lower frequency response are the result of the cogging that behaves like a stiffness with a high variance over the position. The mid-frequency response shows a smooth and identical behaviour over the range of motion. This is expected since the inertia is dominant in behaviour. The higher frequencies, however, show again a variance in behaviour. This is the result of the change in support stiffness of the flexures, which reduces when the system is in a deflected state. This has a non-colocated pole as result and has to be taken into account for the controller design.

The behaviour of the system at $0\ \mathrm{rad}$ is taken as the average system behaviour in order to fit a nominal system for the control design. On this behaviour, a second order plant has been fitted. Fig. 20 illustrates the comparison between the measured behaviour and the estimation. The identified plant is

$$G(s) = \frac{1}{0.2s^2 + 0.74s + 11.46}. \tag{31}$$

The values are in system units. These can be converted into SI-units, as done for the mass in section F. The estimated

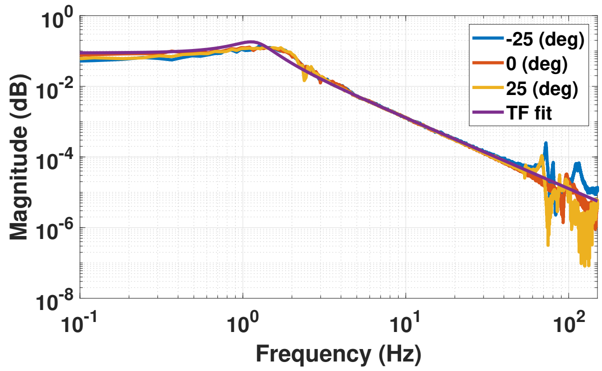

Fig. 20. The frequency response of the system over the entire range of motion.

mass of the plant is $1.46\ \mathrm{kg}$ which is within the accuracy of the current. Therefore the assumption can be made that the plant is correctly identified.

A. Broken Spring

During testing, some of the leaf springs of slaving mechanism, which constrained the inner body of the butterfly hinges broke, releasing a degree of freedom. The system with the unconstrained body is compared to the system with the constrained shown in Fig. 21. The system without the leaf spring has an additional DoF at $19.35\ \mathrm{Hz}$. This shows that the leaf springs to constrain the inner body of the butterfly hinge are necessary. Otherwise, low-frequency parasitic dynamics is introduced, which undermines the bandwidth of a stable controller.

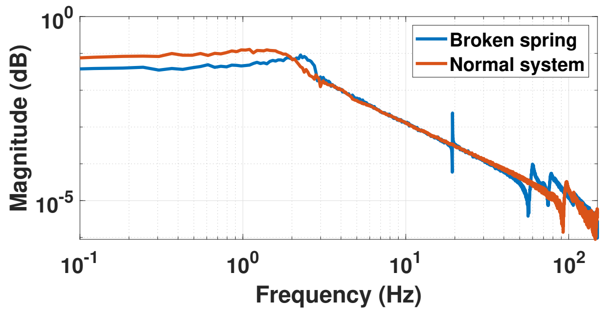

Fig. 21. Comparison between the system with and without leaf springs to constrain the inner body. See the resonance peak at $19.35\ \mathrm{Hz}$.

APPENDIX B
K-FACTOR

The K-factor is the relation between the current and the resulting torque. It is determined by adding mass to the end-effector and measuring the difference in the required current for tracking the same trajectory. The amount of torque required for this additional mass is known and can, therefore, be used for the estimation of the K-factor. The experiment has been done with and without an additional mass of $1.46\ \mathrm{kg}$ attached to the end-effector. In both cases, the same trajectory of $\pm 0.5\ \mathrm{rad}$ at low speed is performed with an identical PID

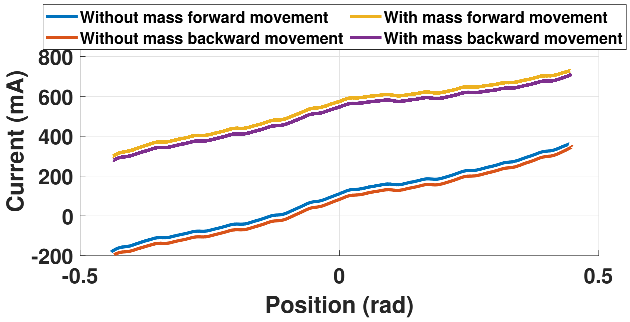

Fig. 22. The difference in required current to perform the motion with and without the additional mass.

controller only with a different K_p to scale for the attached mass. The results are shown in Fig. 22, where one can see that the loops are indeed identical, only shifted due to the additional mass.

In order to calculate the K-factor, the measurement without the mass has to be subtracted from the measurement with the mass. The result is shown in Fig. 23 together with the estimation. The K-factor can be estimated using

$$K_m = 1000 \frac{mgl}{I_{\text{RMS}}} \sin\left(\frac{\theta}{2\pi} + \phi\right). \tag{32}$$

The range of motion limits the amount of sinusoid that can be measured. This makes it difficult to identify the phase of the system. The frequency of gravity is a full rotation, 2π. The weight of the mass is $1.465\ \mathrm{kg}$, the length from the centre of rotation to the centre of mass is $0.187\ \mathrm{m}$ and the gravity constant at the measurement location (Twente, The Netherlands) is $9.813\ \mathrm{m\,s^{-2}}$. The factor 1000 is since the current is expressed in $\mathrm{mA_{RMS}}$ and the K-factor in Ampere. Using a regression, the sinusoid has been fit to the measurement. The measured K-factor is $5.6377\ \mathrm{Nm/A_{RMS}}$. This is higher than specified value of $5.57\ \mathrm{Nm/A_{RMS}}$ [11]. However, the current measurements of the motor driver have a measurement accuracy of 3% [9]. Therefore the measured K-factor with the error bounds of 3% is within the given specifications.

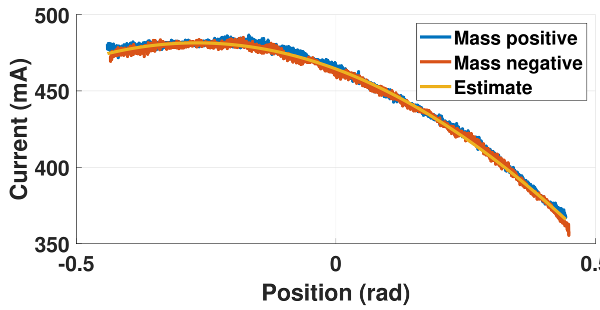

Fig. 23. The measurements compared to the estimated current required to compensate the gravitational forces.

Appendix C
Noise Analysis

The different noise sources within the system have to be identified, so possible improvements to the amount of noise and disturbances can be proposed. First, the position encoder is analysed. After which, the motor driver is analysed.

A. Position Sensor

The position is measured by the Heidenhain LIC-401 [10], which has a resolution of $\pm 2 \cdot 10^{-9}\ \mathrm{m}$ [10]. In order to test if the position sensor is able to measure below the required resolution of $50\ \mathrm{nm}$, the system is held at a fixed location. During the test, the motor drive is only used to measure the position, so the current is turned off and does not influence the system. The measured position noise is $10.5\ \mathrm{nm}$. Fig. 24 shows the frequency content of this measurement, which is almost entirely white. This is higher than the specified value. However, this can be the result of the floor vibrations in combination with the flexures which partially cancel this movement in the system's body resulting in a velocity difference between the floor and the manipulator. Overall, the position sensor's performance is below the required accuracy and does, therefore, not limit the standstill performance of the system.

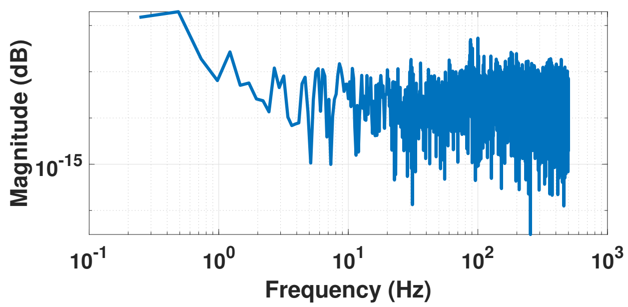

Fig. 24. The frequency response of the fixed system with the motor driver turned off.

B. Motor Driver

For the motor driver, first, the expected current noise and ripple are estimated. After this actual current is measured and compared to the estimated value. Furthermore, different components of the system are checked for their influence on the current noise and ripple.

1) Expected Current Ripple and Noise

The first source of a current ripple produced by the motor drive is PWM voltage signal used to control the desired current. Although it approaches the desired value, it does have a current ripple placed upon it. This ripple is dependent on the voltage bus, the modulation frequency and inductance of the overall system. Grandi [27] has derived an expression to quantify this current ripple

$$i_{\text{pp}}^{\text{max}} = \frac{V_{\text{dc}} T_s}{2\sqrt{3}L} m, \tag{33}$$

which is valid for symmetric SV-PWM method. The Kollmorgen AKD drive has a DC-voltage bus of $320\ \mathrm{V}$ and a PWM frequency of $10.52\ \mathrm{kHz}$ [9]. The method of the PWM signal is unknown, however, assumed to be symmetric SV-PWM.

The motor has a phase-phase inductance of 39 mH [11]. The modulation index, m, is defined as $m = V^*/V_{\mathrm{dc}}$, which makes the current ripple dependent on the reference voltage requested by the current loop.

The expected amplitude of the current ripple caused by the PWM signal is shown in Fig. 25. The moment where the current ripple will be most influential on the system's performance is during standstill, which requires around 500 $\mathrm{mA_{RMS}}$. The current noise during the standstill corresponds to a ripple of 3.5 $\mathrm{mA_{RMS}}$.

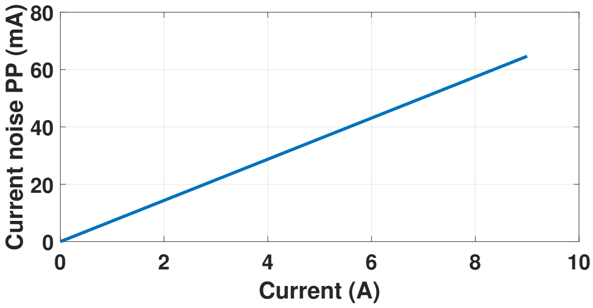

Fig. 25. The expected current ripple over the work range of the motor driver.

Another possible noise source is the current sensors, the LTSR 15-NP by produced by LEM [28], used in the drive. These sensors, which, are used for current measurements on the motor phases have a measurement accuracy of $\pm 0.2\%$ [28] which translates to ± 1 mA error per phase during standstill position. The motor drive utilizes two current sensors to measure the three phases. The third phase, which is not measured, can be calculated using Kirchhoff's current law

$$I_w = -(I_u + I_v). \tag{34}$$

Therefore, the measurement errors in the first two phases also affect the estimated current of the third phase. This error in a single current sensor is, therefore amplified in the RMS current noise. In Fig. 26 the extreme cases for the error are shown, such as the case where one of the two sensors estimate the bottom line of the current and the other overestimates the current. This results in a maximal over- or underestimation of the RMS current by 2 $\mathrm{mA_{RMS}}$. This estimation error has a frequency of 2 Hz per electrical rotation, which translates to the 28$^{\mathrm{th}}$ mechanical harmonic.

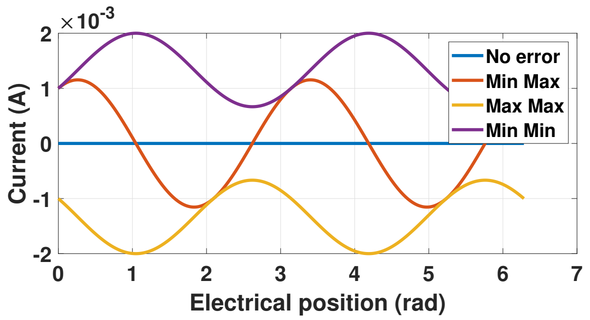

Fig. 26. Fault in RMS current calculation for different sensor faults over one electrical period.

Another element which may cause a ripple is the IGBTs used in the motor driver. These have a leakage current, which is caused by that no transistor is a perfect insulator and will, therefore, always conduct a small amount of charge. In the case of the IGBT's an example, the VS-GT120DA65U by Vishay, was found to have 50 nA as leakage current [29]. This is so small that, even though it may appear on all three phases in an unknown combination, it would not yield to a measurable influence.

The current measurements also suffer from quantization through the ADC converter. A typical ADC has a measurement resolution of 16 bits over the measurement range. The RMS current range of the drive is ± 9 $\mathrm{A_{RMS}}$, which translates to ± 7.33 A for an individual phase. The quantization error therefore is 0.274 mA for an individual phase, which translates to 0.092 $\mathrm{mA_{RMS}}$ for the RMS current.

2) *Measured Current Ripple and Noise*

The measured current ripple, however, is bigger than the expected 5.5 mA by the PWM signal. Fig. 27 shows the measured RMS current ripple over the position. The noise on the current is an input disturbance on the system and, therefore, directly affects the position noise. This correlation can be seen in Fig. 27. The current noise was found to be between 4.5 and 9.5 $\mathrm{mA_{RMS}}$ and have a period of 0.2248 rad, which is equal to the expected 28$^{\mathrm{th}}$ harmonic. The origin of this higher noise level could be noise on the auxiliary power supply, which powers the logic of the drive and the encoder, or the current sensor noise.

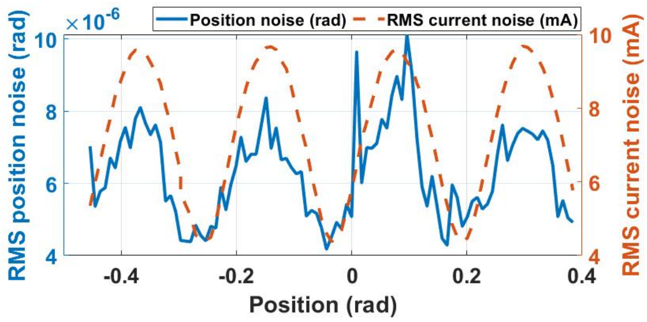

Fig. 27. Voltage produced by the voltage source for the motor driver. Note the 50 Hz noise.

Since the current ripple is higher than the expected 5.5 $\mathrm{mA_{RMS}}$, other elements have to be tested for influence the magnitude of the current ripple.

First, the auxiliary power supply for the motor driver logic is tested if it influences the current noise. The measured voltage supplied by the power supply is depicted in Fig. 28. The power supply indeed has a noise of 76 mV on the output voltage, which is found to be caused by a 50 Hz source. Therefore, to determine if this voltage noise influences the system's performance, the power supply was replaced with a battery pack which supplied the voltage without the noise. This, however, did not affect the amount of noise on either the position or current. Therefore, it can be concluded that the auxiliary power supply does not influence the current or position noise.

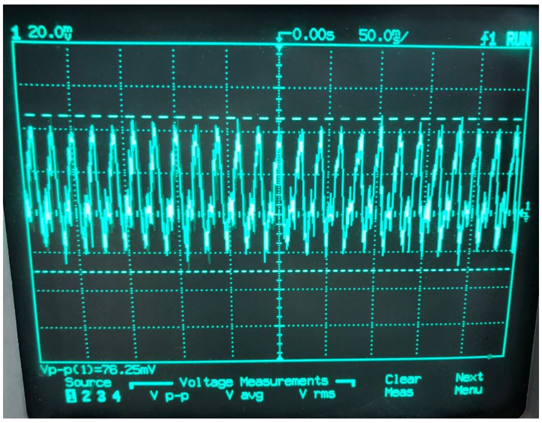

Fig. 28. Voltage produced by the voltage source for the motor driver. Note the 50 Hz noise.

Second, to determine if the current noise indeed originates from the motor driver, a commutation error has been set into the drive. This leads to the drive thinking that the electrical phase is ϕ degrees away. The shape of both the current noise and the position noise shifted along with ϕ. Therefore, the conclusion can be made that the motor drive indeed causes the current and position noise.

The overall conclusion regarding the current ripple is that the motor drive behaves as specified. However, the design does not meet the requirements of the setup. The manufacturer specifies a current accuracy of 3% [9], which is met. The PWM and sensor noise have explained most of the current noise. The remaining part may be an indication that there might be an unbalance is present in the system. It is recommended to use a motor driver with better performance and especially regarding the current noise since this is the primary noise source of the overall system and limiting its performance.

Appendix D
Cogging

One of the disturbances within the system is the cogging. The cogging is defined as the torque ripple present without any current supplied. This torque ripple is generated by the interaction between the rotor's magnetic flux and the angular variations in the stator magnetic reluctance[24]. The slots in the iron and the varying magnetic field cause a difference in permeability path over the rotation. This results in a torque which is dependent on the position and is a consequence of the geometry of the PMSM. The cogging torque can be up to 3% of the rated motor torque, according to Grcar et According to Islam et al., the native harmonics of the cogging, which are the harmonics originating from the motor design, follows from the number of magnets and coils present in the motor [30]. The PMSM used in the system has 28 magnets, N_{mag}, and 21 coils, N_{coils} spread evenly over the rotation [11]. Its resulting native harmonics are calculated using al [31].

According to Islam et al., the native harmonics of the cogging, which are the harmonics originating from the motor design, follows from the number of magnets and coils present in the motor [30]. The PMSM used in the system has 28 magnets, N_{mag}, and 21 coils, N_{coils} spread evenly over the rotation [11]. Its resulting native harmonics are calculated using

$$H_{\text{cogging}} = \text{LCM}(N_{\text{mag}}, N_{\text{coils}}) \cdot i \tag{35}$$

where LCM is the least common multiple of the number of magnet poles and coils and, $i = 1,\ 2,\ 3\ ,....$ The LCM equals 84 resulting in a base harmonic of 0.0748 rad. This first harmonic is frequency is expected to contain the largest amount of energy and therefore of the most interest.

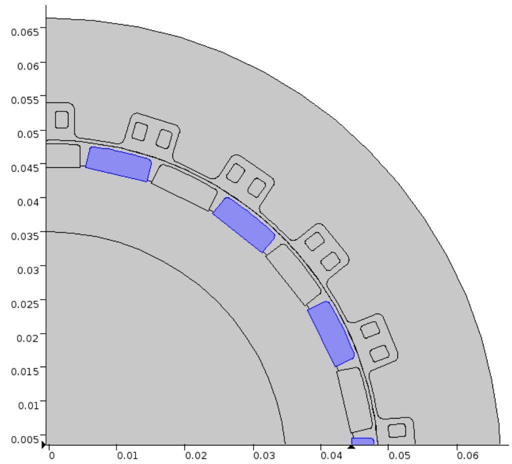

Fig. 29. Overview of the geometry designed in Comsol. All the known parameters of the PMSM are used. The unknown parameters are estimated others are estimated.

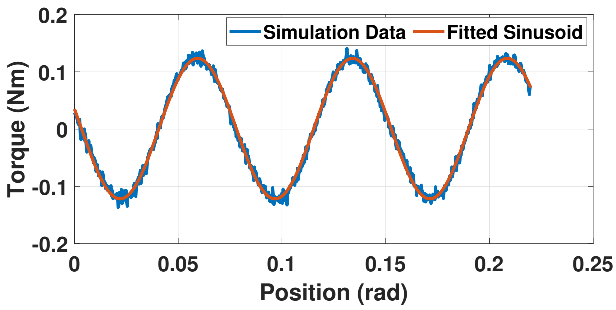

Fig. 30. Result of the numerical analysis, which indeed shows the expected harmonics.

For a better indication, if the analytical analysis is accurate, a 2D FEM simulation is done using COMSOL Multiphysics [32]. The model is constructed corresponding with the specification in the specsheet [11]. However, since most of the parameters of the motor are unknown, these parameters, such as the coil size and placement, have to be estimated. Therefore, the amount of correspondence for the higher harmonics is expected to be low, since these are the result of parameters such as tooth width or skewing [33]. The simulation is calculated over a rotation of 0.22 rad with no current applied to the stator. The magnets have a strength of 0.84 T, which is chosen arbitrarily.

Fig. 30 shows the results of the FEM simulation. These clearly show a sinusoidal cogging shape with some minor numerical noise. The cogging found using the numerical analysis has a period of 0.747 rad, which is close to the analytical value. The small difference of 0.001 rad can the result of simulating only 2.5 periods in combination with the numerical noise from the simulation. Therefore, the conclusion is drawn that they yield the same results and that the 84^{th} is indeed the first harmonic related to the motor design. An interesting remark is that the numerical simulation did not show any other harmonics than the first harmonic predicted by the analytical approach. This may be the result of the motor design or elements such as 3D space which are not included in the simulation. Furthermore, in the real PMSM fabrication error are present. It is, therefore, expected that in the cogging found on the real system will have other harmonics.

Lastly, the cogging on the real system is estimated. The movement on the system was performed similarly to section B. For the cogging estimation, first the current related to the gravitational forces, see section B, is subtracted from the measurement. Next, the linear component of the current, which is related to the stiffness of the flexures, is subtracted. The remaining current has zero mean, which matches with the definition of the cogging [24]. The remaining current is, therefore, related to the cogging. The estimated cogging is

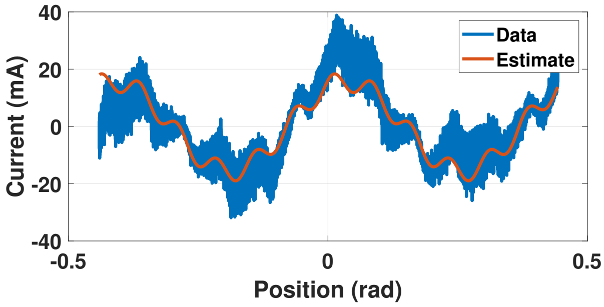

Fig. 31. The measured cogging of the real system and the fitted estimated of the cogging.

illustrated in Fig 31. It does indeed contain a sinusoid with the 84^{th} harmonic as predicted by the analytical and numerical analysis. However, also, other components have been found. Černigoj et al. [34] mentioned that other harmonics could originate from production irregularities, for example, magnet or stator misplacements. These production irregularities can cause harmonics which have the number of poles, magnets or the interlocks in the back-iron in the stator as base harmonic [35]. The measured harmonic turned out to be the 7^{th} harmonic, which is predicted by the greatest common devider (GCD) which is equal to 7 and is equal to 4π electric or 2π mechanical. This harmonic has a mechanical origin. The combination of the 7^{th} with the 84^{th} is included in Fig 31. The difference in the estimate and the data can originate from different elements. First, the amplitudes of harmonics are affected by the combination between the magnet and coil. A different combination in the same phase may lead to a different torque. Second, the lockings of the back iron in the stator may influence the cogging. Third, the stiffness of the flexures is assumed to be linear. However, it does show a difference of 5%, which leads to an error. Last, The flexures have a pivot-shift which alters the cogging. An example in literature showed a change of 20% [33] as a result of the pivot shift.

The cogging has successfully been identified. An analytical and numerical approach showed to be able to estimate one of the two primary harmonics of the cogging.

Appendix E
Repeatabillity

One of the key points of the system is its expected, highly deterministic nature and high repeatability. This is one of the components which has to be tested. The full motion range is tested and begins at -0.4625 rad ($-26.50°$) and stops at 0.4625 rad ($26.50°$) after which the motion is repeated in opposite direction. This is repeated for ten times. The movement is done at $10°\ \text{s}^{-1}$. Fig. 32 shows the requested currents by the controller over the position for 10 movements plotted over one another. The differences between the different motions is around $5\ \text{mA}_{\text{RMS}}$, which is mainly related to the noise. The system, therefore, indeed shows its expected deterministic behaviour. However, Fig. 32 also shows a hysteresis in the system, which is expected to be from an electrical origin. Fig. 33 shows the hysteresis over the position, which is calculated by subtracting the backward motion from the forward.

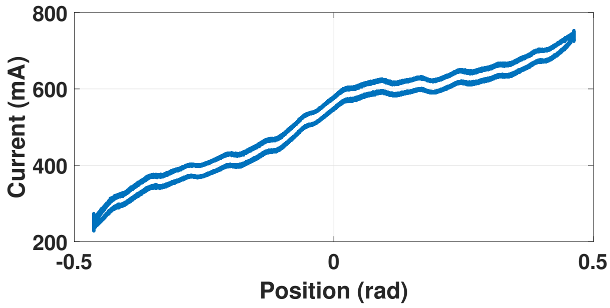

Fig. 32. Requested current by the controller for a $1\ \text{deg/s}$. Note the minimal variance in the current.

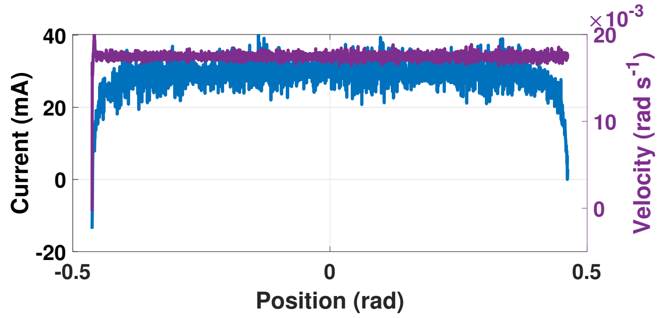

Fig. 33. Difference in requested current between forward and backward motion (blue). Together with the velocity (purple)

In order to find if the hysteresis is velocity dependent, the motion described earlier is repeated at different velocities. It is expected that this would yield a similar result since there is no expected velocity component, which influences the behaviour of the system. Fig. 34 shows that at velocities below $100^\circ\ \mathrm{s}^{-1}$ the system indeed behaves identical, however at higher velocities the forward motion and backward motion no longer have an identical shape, see Fig. 35. At velocities of $250^\circ\ \mathrm{s}^{-1}$ a harmonic arises which only becomes larger at higher speeds. The harmonic is the result of that at these higher velocities, the effect of the harmonics of the cogging become larger. At higher velocities, the harmonics may rise above the bandwidth of the feedback controller. The highest frequency component of the cogging is found to be the 84$^{\text{th}}$ harmonic. At a velocity of $250^\circ,\ 500^\circ,\ 1000^\circ\ \mathrm{s}^{-1}$ the frequencies in time domain become, respectively, $5.8,\ 11.6,\ 23.8$ Hz. This, in combination with the delay of 3 time samples, results in a bigger error on the position and velocity and the current applied by the feedback controller.

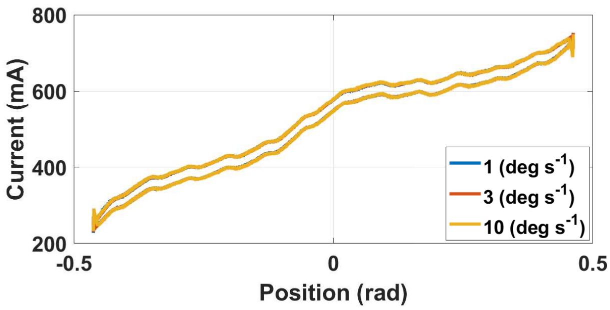

Fig. 34. Requested current for forward and backward motion at low velocities. Note the hysteresis loop.

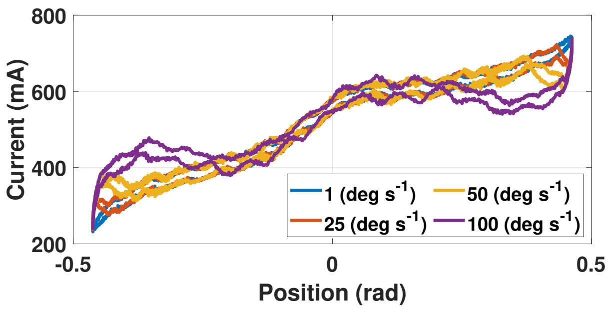

Fig. 35. Difference in requested current between forward and backward motion at high velocities. Differences at begin and end position are related to the accelations of the system.

These higher speeds can, therefore, not be used to estimate the hysteresis, since the current shows the effect of the cogging, which makes the hysteresis unreliable. The current model shows that the hysteresis has an amplitude of $15\ \mathrm{mA_{RMS}}$, which is only present during a motion. The model is expressed as

$$I_{\text{hyst}} = 15\tanh(\omega), \tag{36}$$

where ω is the velocity of the system and $\tanh$ is the tangent hyperbolic.

The hysteresis loop has been identified. However, its origin remains uncertain. The acceleration of the system, which was limited at $5000^\circ\ \mathrm{s}^{-2}$, at the beginning and end of the motion, can be used to gain some insight if it is dependent on the force or velocity. As shown in Fig. 36, the difference in the forward and backward motion remains equal even though the system is accelerating. The harmonics present during the higher velocities are the result of the frequency being higher than the bandwidth of the controller. However, the average current remains equal. Therefore it can be concluded that the hysteresis is not dependent on the force or acceleration.

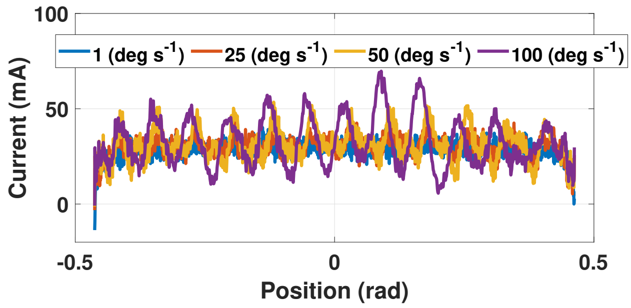

Fig. 36. The hysteresis loop of the requested current at different velocities. Low frequency components are related to the cogging.

Appendix F
Unit Conversion

The estimated values, such as the system's inertia, are expressed in system units. This is relatively difficult to comprehend and, therefore, the parameters are converted to SI units. The measured position is in degrees, which can be converted to radials using

$$x_{\text{rad}} = \frac{\pi}{180} x_{\text{deg}}. \tag{37}$$

And the required torque to position the system is expressed in milliampere. This has to be converted to newton meter using

$$\tau = \frac{K_m}{1000} I_{\text{RMS}}, \tag{38}$$

where K_m is the motor constant, the division by 1000 is since the motor constant is defined as torque per ampere. The transfer function estimated in Eq. (31) with $\mathrm{mA_{RMS}}$ as input and degrees as output has to be converted to the SI units specified earlier. The conversions presented above are applied here

$$Y(s) = \frac{\pi}{180} \frac{1}{0.2s^2 + 0.76s + 11.46} \frac{1000}{K_{\text{m}}} X(s), \tag{39}$$

which results in

$$Y(s) = \frac{1}{0.0642s^2 + 0.0735s + 3.6449}. \tag{40}$$

The system's inertia is found to be equal to $0.0642\ \mathrm{kg\,m^2}$. The stiffness is equal $3.6449\ \mathrm{N\,m\,rad^{-1}}$. To calculate the weight of the system, the inertia has to be converted using

$$I_{\text{total}} = I_{\text{rotor}} + I_{\text{beam}}, \tag{41}$$

where the inertia of the rotor, I_{rotor} is equal to $0.005\ \mathrm{kg\,m^2}$. The inertia of the added beam is defined by three components. First, rotations of the center of mass (CoM). Second, rotation around a different point than the CoM in the x-direction. And, last, rotation around a different point than the CoM in the z-direction

$$I_{\text{beam}} = \frac{1}{12}mL^2 + md_x^2 + md_y^2, \tag{42}$$

where the inertia of a beam is calculated and through the parallel axis theorem the influence of the shift. The parameter M is the mass of the system. L is the length of the beam, which is 0.20 m. d_x, and d_y are the distances between the centre of mass and the centre of rotation, which is equal to 0.187 m and 0.05 m. Using the estimated inertia of the system, the weight of the beam is estimated to 1.4510 kg. The estimated mass matches the measured mass of the beam.